Mohamed Khider University of Biskra
Faculty of Exact Sciences Natural and Life Sciences
Material Sciences Department

MASTER'S DISSERTATION

Material Sciences
Physics
Condensed Matter Physics

Ref:

Presented by:
Lehmaidi Assil

At: 2024-06-11

Elaboration and Characterization of Local Ceramic Materials for Agricultural Microfiltration Applications

---

Jury:

Mrs.	Harzallah Wahiba	MCB	University of Biskra	President
Mr.	Boukhemis Boudaira	MCA	University of Biskra	Supervisor
Prof.	Mohamed Toufik Soltani	PROF	University of Biskra	Examiner

Academic Year: 2023-2024

Dedication

In fond memory of my father, Mohamed Lehmaidi,

For being my guiding light and endless inspiration.

I dedicate this work to you.

-Assil Lehmaidi

Acknowledgements

First and foremost, I express my deepest gratitude to Allah the Almighty, whose guidance, mercy, and wisdom have been the ultimate source of strength and inspiration throughout my studies.

I express my deepest gratitude to *my mother*, whose unwavering support and encouragement have been my foundation throughout this journey. Her boundless love has been a constant source of strength.

To my family, thank you for your understanding and patience. Your collective support has made this accomplishment possible.

Special thanks to my supervisor *Dr. Boukhemis Boudaira* for his guidance, expertise, and invaluable feedback. His mentorship has been instrumental in shaping the trajectory of this work.

A heartfelt appreciation goes to *Tarek Melki* for generously sharing his insights and experiences, providing valuable guidance that significantly contributed to the development of this project.

I extend my gratitude to CRSTRA - OMAR EL BERNAOUI and *Prof. Bouchahm Nora* for their collaboration and providing access to their labs. This partnership has played a pivotal role in the successful execution of my research.

Special acknowledgment to *Youcef Bouzidi* for his exceptional skills, which has greatly contributed to the success of this endeavor.

And a special thanks to BISKRIA CEMENT and *Amrani Belkacem* for their invaluable assistance, particularly in conducting the necessary analysis for this project.

I am indebted to my friends, *Chouaib Azzouz, Ahmed Ramdane Amamra & Sami Ben Medjeddel, Khalil Ziani, Mohamed Mouadh Messaoui, Abbes Ben Adel, Saber, Hamza, and all of my classmates* whose camaraderie and encouragement have brightened even the most challenging moments. Your friendship has been a vital part of this experience.

Thank you all for being integral parts of my academic journey.

Table Of Contents

Table of Contents

List of Tables

List of Figures

List of Figures

List of Graphs

General introduction

The ceramic products are extremely interesting in the field of the membrane supports because of their mechanical resistance, chemical inertia, long working life, and thermal stability. [1]

The purpose of this study is to make membrane supports, A membrane support provides mechanical strength to a membrane top layer to withstand the stress induced by the pressure difference applied over the entire membrane and must simultaneously have a low resistance to the filtrate flow.[1]

Membrane technology is used in the water industry to improve the quality of water for use, reuse, or discharge to the environment. Membranes range from finely porous structures to nonporous and can remove contaminants such as bacteria and protozoa down to ions. This chapter describes the role of membrane technology in the water industry, how membranes are made and tested, the types of modules used to house the membranes, and the basic relationships describing performance and operational aspects including energy usage and costs. [2]

The first introductory chapter provides a comprehensive overview of ceramic materials, delving into their diverse types, intricate structures, defining characteristics, and wide-ranging applications within various industries. This exploration leads us to an in-depth discussion on membrane technology. Then we transition to expand upon membrane definitions, classifications, and the fundamental processes of microfiltration and ultrafiltration. Additionally, it delves into the crucial concept of membrane supports, investigating their different configurations and the different manufacturing methods employed to create them.

In the second chapter, considerable attention is devoted to the analysis of raw materials, starting from their precise sourcing locations to the intricate processes of grinding, calcination, and sieving. This section not only outlines the methodologies employed but also emphasizes the importance of each step in ensuring material quality and consistency. Furthermore, the chapter delves into various chemical analyses, including Fourier Transform Infrared Spectroscopy (FTIR), Thermogravimetric Analysis/Differential Scanning Calorimetry (TGA/DSC), X-Ray Diffraction (XRD), and X-Ray Fluorescence (XRF). The conclusions drawn from these analyses form a critical foundation for subsequent stages of the research.

The third chapter outlines the fabrication process, from the meticulous preparation of the mixture to the precise creation of the paste. It then progresses to the intricate techniques of extrusion fabrication, followed by the procedures of drying and heat treatment. Each step is methodically explored, highlighting the crucial parameters and techniques employed to ensure the production of high-quality membrane supports.

In the fourth and final chapter, a comprehensive analysis of results is undertaken, encompassing a wide array of methodologies. This includes detailed examinations of chemical analyses such as XRF and XRD, thorough examination of SEM images, and rigorous assessments of mechanical properties. Additionally, permeability and filtration attributes are meticulously evaluated, providing crucial insights into the performance of the membrane supports. These findings are contrasted with existing literature, allowing for a comprehensive understanding of the research's significance and implications within the broader scientific community.

Chapter I: Introduction To Ceramics and Membrane Technology

I.1. Introduction

Membranes have gained an important place in chemical technology and are used in a broad range of applications. The key property that is exploited is the ability of a membrane to control the permeation rate of a chemical species through the membrane. In controlled drug delivery, the goal is to moderate the permeation rate of a drug from a reservoir to the body. In separation applications, the goal is to allow one component of a mixture to permeate the membrane freely, while hindering permeation of other components.[3]

And to this end ceramic materials have been chosen as the base for making these membranes. the use of ceramic membranes has many advantages such as high thermal and chemical stability, pressure resistance, long lifetime, and good antifouling properties.[4], [5]

I.2. Ceramics

I.2.1. Definition of Ceramics

Ceramics can be defined as solid compounds that are formed by the application of heat, and sometimes heat and pressure, comprising at least two elements provided one of them is a non-metal or non a nonmetallic elemental solid. The other element(s) may be a metal(s) or another nonmetallic elemental solid(s), A somewhat simpler definition was given by Kingery who defined ceramics as, “the art and science of making and using solid articles, which have, as their essential component, and are composed in large part of, inorganic nonmetallic materials” in other words, what is neither a metal, a semiconductor or a polymer is a ceramic. [6]

I.2.2. Traditional Versus Advanced Ceramics

Most people associate the word ceramics with pottery, sculpture, sanitary ware, tiles, etc. And whereas this view is not incorrect, it is incomplete because it considers only the traditional, or silicate-based, ceramics. Today the field of ceramic science or engineering encompasses much more than silicates and can be divided into traditional and modern ceramics.[6]

I.2.2.1. Traditional Ceramics:

- **Composition:** Primarily silicate-based, consisting of clays and feldspars.
- **Microstructure:** Characterized by coarse, porous microstructures, often nonuniform and multiphase.
- **Formation:** Typically formed by processes like slip casting or potter's wheel shaping.
- **Firing:** Fired in a flame kiln to sinter the materials.
- **Properties:** Generally porous, limited in strength and density.

- **Applications:** Commonly used for pottery, sculptures, tiles, and traditional household items.
- **Historical Significance:** Has a long history dating back to the dawn of civilization, initially used for practical purposes like storing liquids.

I.2.2.2. Modern (Advanced) Ceramics:

- **Composition:** Utilizes more sophisticated raw materials, such as binary oxides, carbides, perovskites, and entirely synthetic compounds.
- **Microstructure:** Microstructures are significantly finer, more homogeneous, and less porous compared to traditional ceramics.
- **Formation:** Formed using advanced manufacturing techniques.
- **Firing:** May involve specialized firing processes tailored to the specific material composition.
- **Properties:** Exhibits superior strength, hardness, and density compared to traditional ceramics.
- **Applications:** Used in high-tech industries such as aerospace, electronics, and biomedical engineering.
- **Historical Significance:** Represents a more recent stage of development, driven by technological advancements and industrial innovation.

In summary, traditional ceramics are characterized by their historical origins, reliance on silicate-based compositions, and relatively simple manufacturing processes. In contrast, modern ceramics leverage advanced materials and manufacturing techniques to achieve superior performance and cater to diverse high-tech applications in contemporary industries.

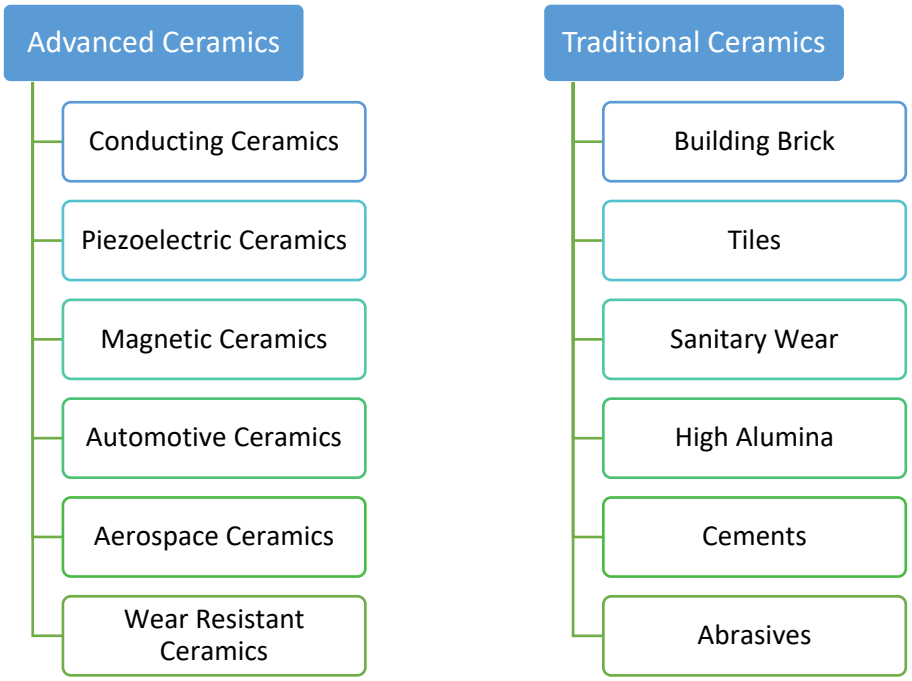

Figure I.1 Examples of Traditional and Advanced Ceramics [24]

I.2.3. Bonding in Ceramics

Ceramics, in a broad sense, can be categorized based on whether they are predominantly bonded ionically or covalently:

I.2.3.1. Ionic Ceramics:

Ionic ceramics are distinguished by their ability to form a tightly packed crystalline structure with maximum density. Typically composed of a metallic element and a non-metallic element, this type of ceramic achieves a dense arrangement due to the presence of ionic bonds.

I.2.3.2. Covalent Ceramics:

In contrast, covalent ceramics are characterized by the presence of covalent bonds, facilitating a crystal structure akin to diamond. Formed predominantly from two non-metallic elements, this type of ceramic exhibits a diamond-like structure, promoting high strength and rigidity.

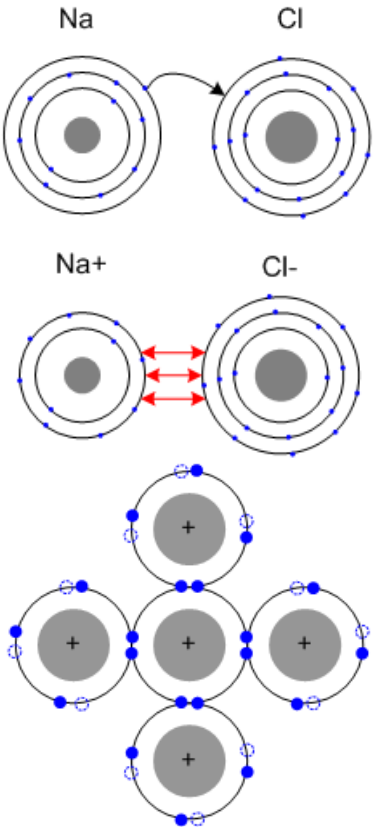

Figure I.2 Ionic and Covalent Bonding (www.substech.com)

I.2.4. General Characteristics of Ceramics

As a class, ceramics are hard, wear-resistant, brittle, prone to thermal shock, refractory, electrically and thermally insulative, intrinsically transparent. nonmagnetic, chemically stable, and oxidation-resistant. As with all generalizations, there will be exceptions; some ceramics are electrically and thermally quite conductive, while others are even superconducting. An entire industry is based on the fact that some ceramics are magnetic.[6]

Hardness and Wear Resistance: Ceramics are known for their high hardness, making them resistant to scratching and abrasion.

Brittleness: They tend to be brittle, meaning they can fracture under stress rather than deform.

High Melting Points: Ceramics typically have high melting points, allowing them to withstand high temperatures without melting.

Chemical and Thermal Stability: Many ceramics exhibit excellent resistance to corrosion and degradation from exposure to harsh chemicals and high temperatures.

Electrical and Thermal Insulation: Ceramics often have low electrical and thermal conductivity, making them effective insulators.

Environmental Friendliness: Ceramics are often composed of abundant natural materials and can be recycled, making them environmentally friendly options in many cases.

I.2.5. Structure And Properties of Some Ceramics

I.2.5.1. Kaolinite

Kaolinite is the most important member of the kaolinite group; dickite and nacrite are rarer polymorphs. The minerals halloysite-10Å and halloysite-7Å are chemically similar to the kaolinites and have compositions with and without interlayer water, respectively. Kaolinite is widely used in the manufacture of bricks and ceramics and also as a coating or filler for papers, paints and plastics.[7]

I.2.5.1.1. Chemical Composition

the formula of kaolinite can be written in terms of oxides as $Al_2O_3.2SiO_2.2H_2O$, that of halloysite is ideally $Al_2O_3.2SiO_2.4H_2O$. In this fully hydrated form of halloysite, 2H2O corresponds with structural (OH) ions and the remainder occurs as interlayer water which is extremely loosely held so that even at room temperature, in an unsaturated environment, most of this water is lost. Thus most, if not all, of the interlayer water is not recorded in the H_2O + values in chemical analysis but appears as H_2O.[7]

In the picture below, the lines are meant to reinforce the idea of the geometries involved: tetrahedra are outlined in blue and octahedra are outlined in green. The bonds between silicon and oxygen are not shown, nor are the bonds between aluminum and oxygen. We have shown the tetrahedra on top and the octahedra below but there really is no top or bottom to the layer, so it can just as easily be drawn the other way around.

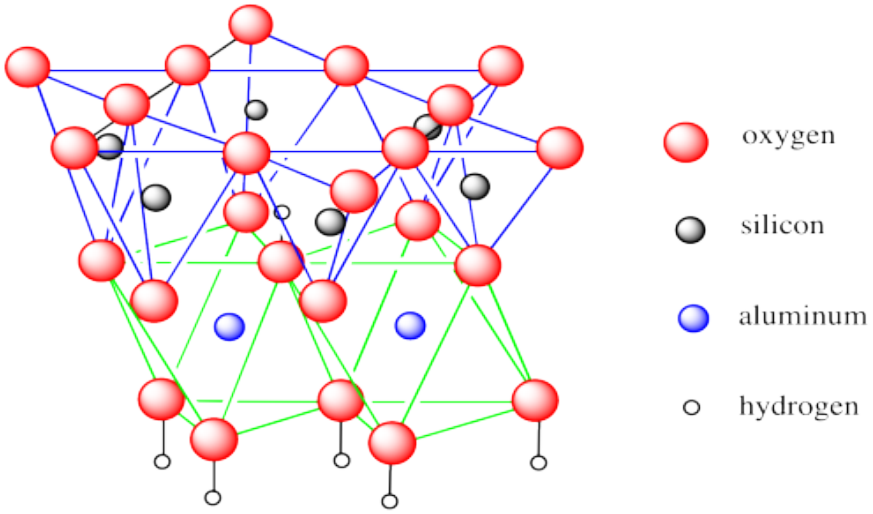

Figure I.3 Kaolinite Crystal Structure: Tetrahedral and Octahedral Geometries[25]

I.2.5.1.2. Occurrence

The principal occurrences of kaolinite are as residual deposits formed by the weathering or low-temperature hydrothermal alteration of feldspars, muscovite and other Al-rich silicates

usually in acid rocks (e.g. granites, rhyolites, quartz diorites). The derivation from feldspar can be expressed as:

$$2KAlSi_3O_8 + 3H_2O \longrightarrow Al_2Si_2O_5(OH)_4 + 4SiO_2 + 2K(OH)$$

Kaolinite also occurs in deposits where it or its parent minerals have been transported under suitable non-alkaline conditions and deposited in deltaic, lagoonal or other non-marine environments. Prime examples of these types of deposits are those of Georgia and South Carolina, USA, which are believed to be derived from the granites and gneisses of the Piedmont plateau.[7]

I.2.5.2. Alumina

Aluminium oxide or alumina (the ceramic) or corundum (the mineral) refers to α-Al_2O_3, it is a hard-wearing material and used throughout many industries. Once fired and sintered, it can only be machined using diamond-grinding methods. Alumina is the most commonly used type of ceramic and is available in purities up to 99.9%. Its combination of hardness, high temperature operation (up to 1,700°C) and good electrical insulation makes it useful for a wide range of applications.[8]

When it is doped with Cr^{3+} the mineral is called ruby; when doped with Ti ions we call it sapphire. Natural sapphire actually contains a combination of Ti^{4+} and Fe^{2+}, which compensate the charge difference.

The crystal structure of Al_2O_3 is trigonal with a $\bar{3}m$ crystal class, and has a pseudohexagonal oxygen sublattice (which is why we usually use a hexagonal cell and four index Miller–Bravais notation) but the symmetry really is 3-fold, not 6-fold. In Al_2O_3 the oxygen ions have what can be thought of as hcp stacking with the Al^{3+} ions occupying two-thirds of the octahedral interstices (balancing the charge).[9]

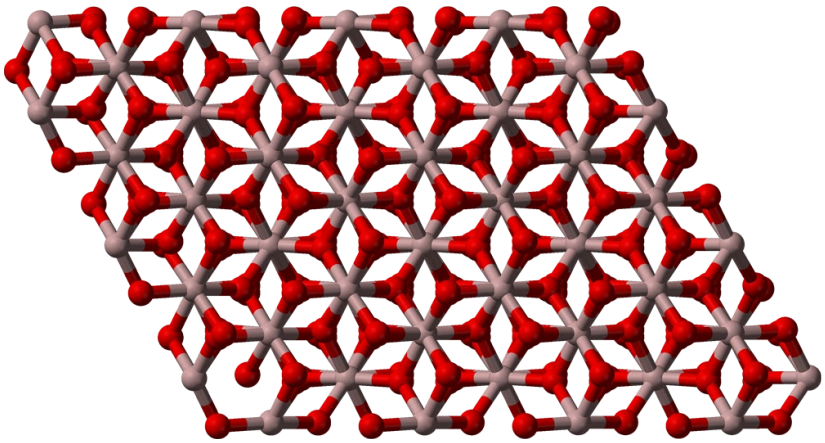

Figure I.4 Ball-and-stick model of part of the crystal structure of corundum, α-Al_2O_3 [26]
Al: *O:*

I.2.5.3. Quartz

Quartz is one of the most abundant minerals and occurs as an essential constituent of many igneous, sedimentary and metamorphic rocks. It is also found as an accessory mineral, and as a secondary mineral in veins and metasomatic deposits. 'Quartz' appears to have replaced the name 'crystal' or 'rock crystal' for this mineral towards the end of the18th Century.

Quartz is the most common natural polymorph of SiO_2. The more important SiO_2 polymorphs and their ranges of stability are:

α-Quartz: stable at ambient temperatures and up to 573ºC.

β-Quartz: stable from 573 to 870ºC. Metastable above 870ºC.

α-Tridymite: metastable from ambient temperatures up to 117ºC

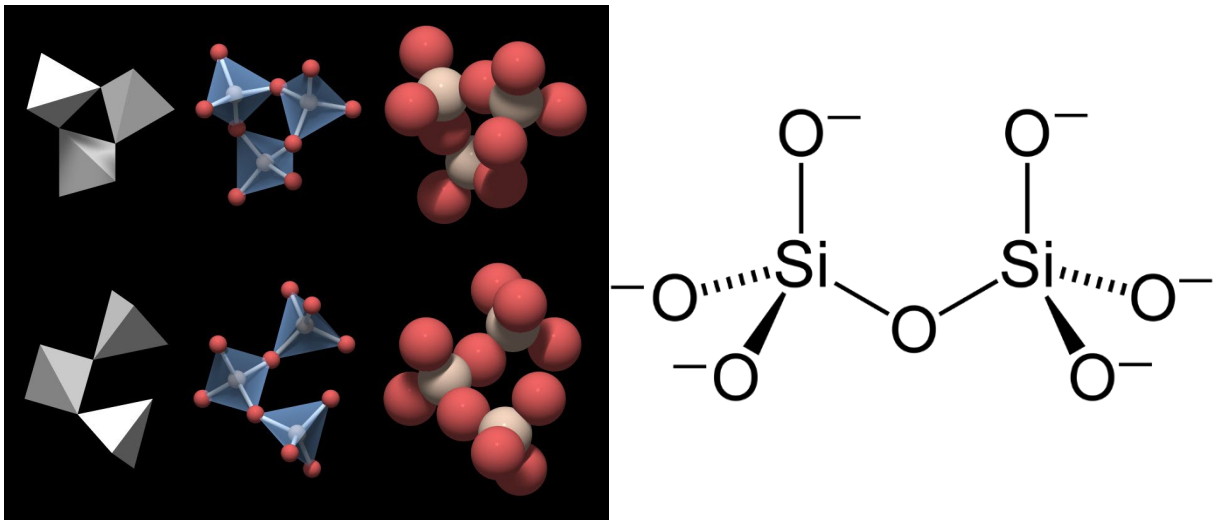

Figure I.5 Basic structural unit of quartz [27]

I.2.5.4. Calcium Carbonate ($CaCO_3$)

Calcium carbonate -Generally not consider a ceramic- is a chemical compound with the formula ($CaCO_3$) formed by three main elements: carbon, oxygen, and calcium. It is a common substance found in rocks in all parts of the world (most notably as limestone), and is the main component of shells of marine organisms, snails, coal balls, pearls, and eggshells. ($CaCO_3$) exists in different polymorphs, each with specific stability that depends on a diversity of variables.

Calcium carbonate boasts several valuable properties such as high brightness, opacity, and thermal conductivity, making it indispensable across numerous industries. It finds applications in powder paint, paper, cosmetics (particularly in toothpaste and makeup), and household products, where it serves as a thickening agent and may substitute for titanium dioxide. Additionally, calcium carbonate is utilized in building, construction, iron and steel, water treatment, and oil and gas sectors, where it minimizes filtration losses in drilling fluids.

In the plastics industry, it enhances the breathability of films used in hygienic or medical products.

I.2.6. Applications of Ceramics

The applications for these materials are diverse, from bricks and tiles to electronic and magnetic components. These applications use the wide range of properties exhibited by ceramics. Some of these properties are listed in *Table I-1* together with examples of specific ceramics and applications. The functions of ceramic products are dependent on their chemical composition and microstructure, which determines their properties. It is the interrelationship between structure and properties that is a key element of materials science and engineering.[9]

Table I.1 Ceramic Applications Overview [9]

Property	*Example*	*Application*
Electrical	$Bi_2Ru_2O_7$	Conductive component in thick-film resistors
	Doped ZrO_2	Electrolyte in solid-oxide fuel cells
	Indium tin oxide (ITO)	Transparent electrode
	SiC	Furnace elements for resistive heating
	$YBaCuO_7$	Superconducting quantum interference devices (SQUIDs)
	SnO_2	Electrodes for electric glass melting furnaces
Dielectric	α-Al_2O_3	Spark plug insulator
	$PbZr_{0.5}Ti_{0.5}O_3$ (PZT)	Micropumps
	SiO_2	Furnace bricks
	$(Ba,Sr)TiO_3$	Dynamic random access memories (DRAMs)
	Lead magnesium niobate (PMN)	Chip capacitors
Magnetic	γ-Fe_2O_3	Recording tapes
	$Mn_{0.4}Zn_{0.6}Fe_2O_4$	Transformer cores in touch tone telephones
	$BaFe_{12}O_{19}$	Permanent magnets in loudspeakers
	$Y_{2.66}Gd_{0.34}Fe_{4.22}Al_{0.68}Mn_{0.09}O_{12}$	Radar phase shifters
Optical	Doped SiO_2	Optical fibers
	α-Al_2O_3	Transparent envelopes in street lamps
	Doped $ZrSiO_4$	Ceramic colors
	Doped (Zn,Cd)S	Fluorescent screens for electron microscopes
	$Pb_{1-x}La_x(Zr_zTi_{1-z})_{1-x/4}O_3$ (PLZT)	Thin-film optical switches
	Nd doped $Y_3Al_5O_{12}$	Solid-state lasers
Mechanical	TiN	Wear-resistant coatings
	SiC	Abrasives for polishing
	Diamond	Cutting tools
	Si_3N_4	Engine components
	Al_2O_3	Hip implants
Thermal	SiO_2	Space shuttle insulation tiles
	Al_2O_3 and AlN	Packages for integrated circuits
	Lithium-aluminosilicate glass ceramics	Supports for telescope mirrors
	Pyrex glass	Laboratory glassware and cookware

I.3. Membranes

I.3.1. The Definition of Membranes

In essence, a membrane is essentially a discrete, thin interface that regulates the permeation of chemical species in contact with it. This interface can be molecularly homogeneous, meaning it is completely uniform in composition and structure, or it may be chemically or physically heterogeneous. For example, it may contain holes or pores of finite dimensions or consist of some form of layered structure. While a typical filter fits this definition of a membrane, the term 'filter' conventionally refers to structures that separate particulate suspensions larger than 1–10μm.[3]

I.3.2. Types of Membranes

I.3.2.1. Symmetric Membranes

- **Microporous Membranes:** These have small, interconnected pores (0.01–10μm) that selectively allow molecules to pass based on size. Larger particles are entirely rejected, while smaller ones may partially pass. They are used for ultrafiltration and microfiltration.
- **Nonporous, Dense Membranes:** comprised of a dense film where permeants move through via diffusion. Separation depends on the relative transport rate determined by diffusivity and solubility. Commonly used in gas separation, pervaporation, and reverse osmosis.

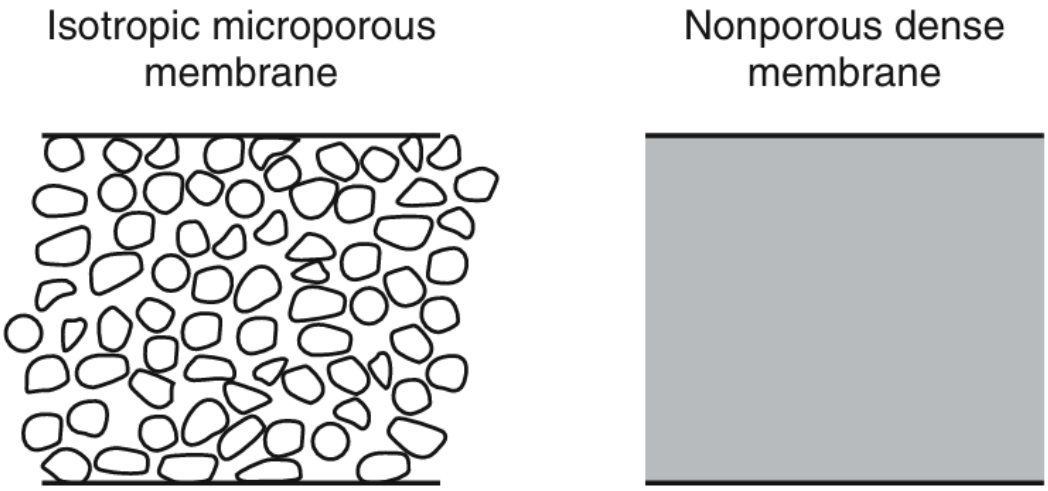

Figure I.6 Symmetric Membranes [3]

I.3.2.2. Asymmetric Membranes:

Anisotropic membranes mark a significant advancement in membrane technology, featuring a thin surface layer supported by a thicker, porous substructure. The surface layer dictates the separation properties and permeation rates, while the substructure offers mechanical support. Compared to symmetric membranes, asymmetric membranes provide higher fluxes owing to

their thin surface layer. This attribute boosts their efficiency and renders them extensively employed in various commercial processes.[3]

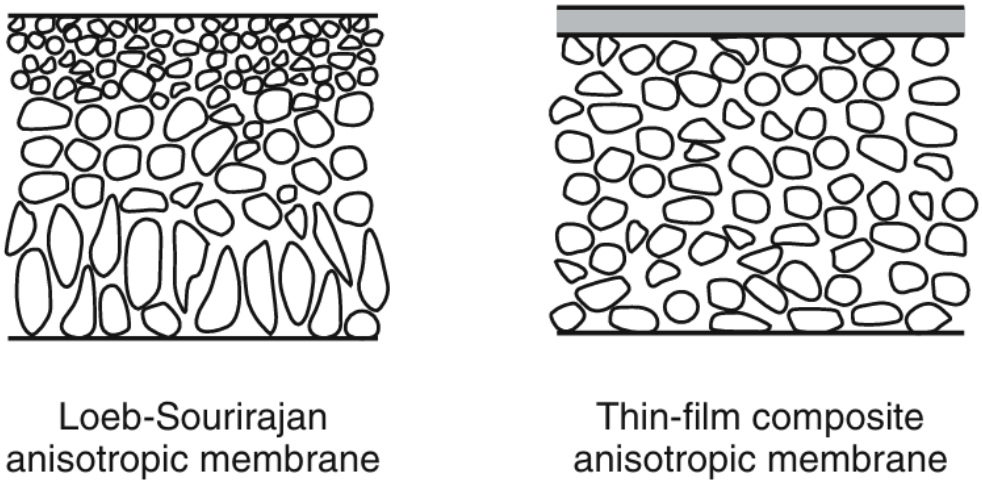

Figure I.7 Anisotropic Membranes [3]

I.3.2.3. Ceramic Membranes

Ceramic membranes offer robust solutions for separation processes requiring durability and stability in harsh conditions. Composed of inorganic materials, they excel in applications such as ultrafiltration and microfiltration, providing enhanced resistance to solvents and high temperatures. Emerging trends include the exploration of dense metal membranes, such as palladium, for specialized tasks like hydrogen separation. With superior mechanical strength and chemical resistance, ceramic membranes are driving innovation in diverse industrial sectors.[10]

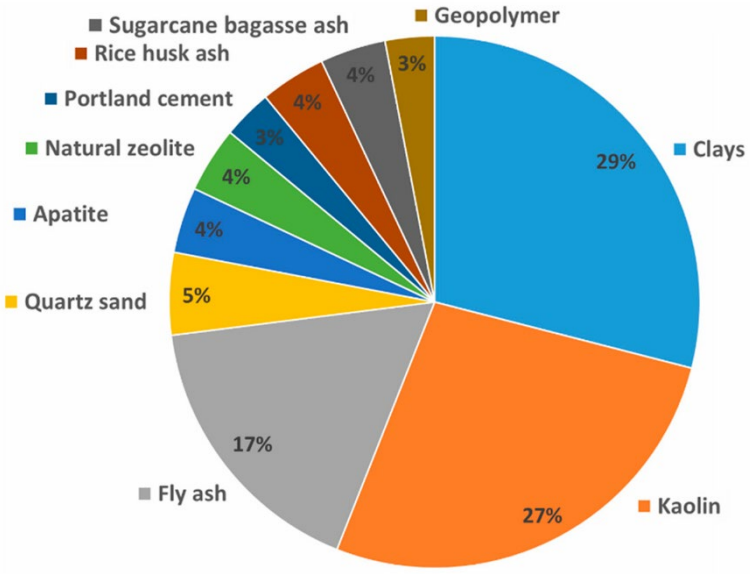

Figure I.8 Representation of different raw materials in studies of low-cost inorganic filtration [28]

I.3.3. Microfiltration

Microfiltration (MF) is a pressure-driven separation process, which is widely used in concentrating, purifying or separating macromolecules, colloids and suspended particles from solution. MF membranes typically have nominal pore sizes on the order of 0.1–1.0 µm. MF

processing is widely used in the food industry for applications such as wine, juice and beer clarification, for wastewater treatment, and plasma separation from blood for therapeutic and commercial uses. In biotechnology industries, MF concerns applications such as cell recycle and harvesting, separation of recombinant proteins from cell debris, and purification of process streams. MF is usually operated at relatively low TMPs (<4 bar or 0.4 MPa) in a cross-flow configuration. [11]

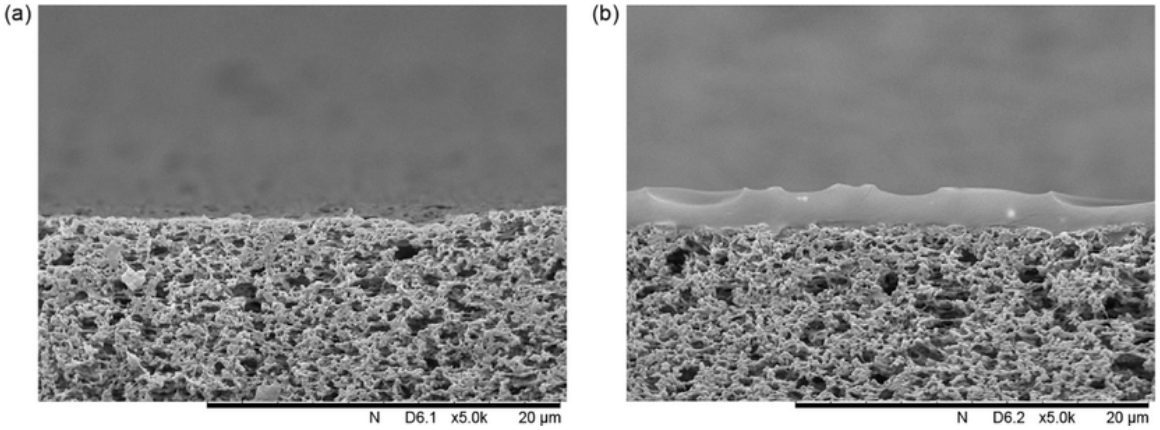

Figure I.9 SEM image of: (a) Non-modified microfiltration membrane (MFFK-1), (b) composite poly(1-trimethylsilyl-1-propyne) (PTMSPM) with MFFK-1 support. [29]

I.3.4. Ultrafiltration

UF membrane separation falls between NF and MF with a pore size range of 0.001–0.05 µm. Both UF and MF membranes are porous in nature, but UF membranes virtually always have an asymmetric structure with a much denser skin layer, i.e. a smaller pore size and lower surface porosity that produces higher hydrodynamic resistance. The thickness of the top layer is 1.0–3.0 µm. Since the osmotic pressure of microsolutes is low or negligible and the pore size is larger than RO and NF membranes, UF operating pressure is low and in the range of 2–5 bar. In the case of solutions containing particles or macromolecules. [12]

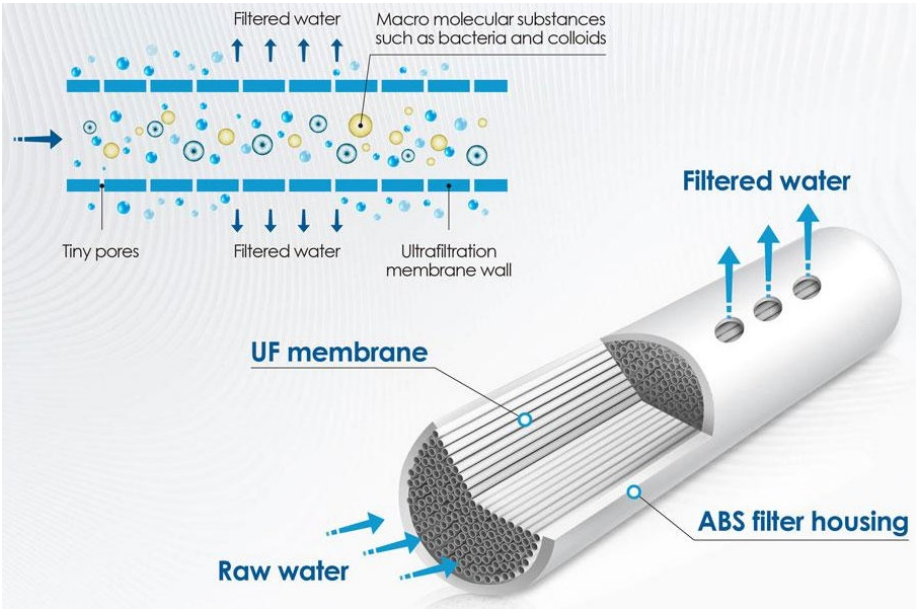

Figure I.10 A diagram that shows microfiltration thin layer and setup [30]

I.3.5. Reverse Osmosis

Is a process where a solution is pressurized against a solvent-selective membrane, surpassing the osmotic pressure difference across it. Typically, water serves as the solvent, while solutes can be salts or organic compounds. Initially applied on an industrial scale for desalting seawater and brackish water, RO has become a key aspect of modern membrane technology. Its efficiency, durability, and decreasing costs have contributed to its success. For instance, RO plants can produce potable water for less than $\$1/m^3$, including all expenses. Seawater, containing around 3.5 wt% Total Dissolved Solids (TDS), can be treated using RO systems operating at 50 to 70 bars, consuming less than 10 kWh of energy per cubic meter of potable water with less than 0.05 wt% TDS. This energy efficiency, compared to multistage flash distillation, has favored RO economically, even for large capacities up to 75,000 m^3/day. RO's market share has increased over the last two decades, facilitated by rising energy costs and competitively priced membrane systems. In seawater RO systems, energy-recovery turbines are utilized to reclaim energy from the high-pressure brine stream. For locations with very high salinity seawater (>4.5% TDS), such as those in the Middle East, desalination systems operate at approximately 80 bars. [13]

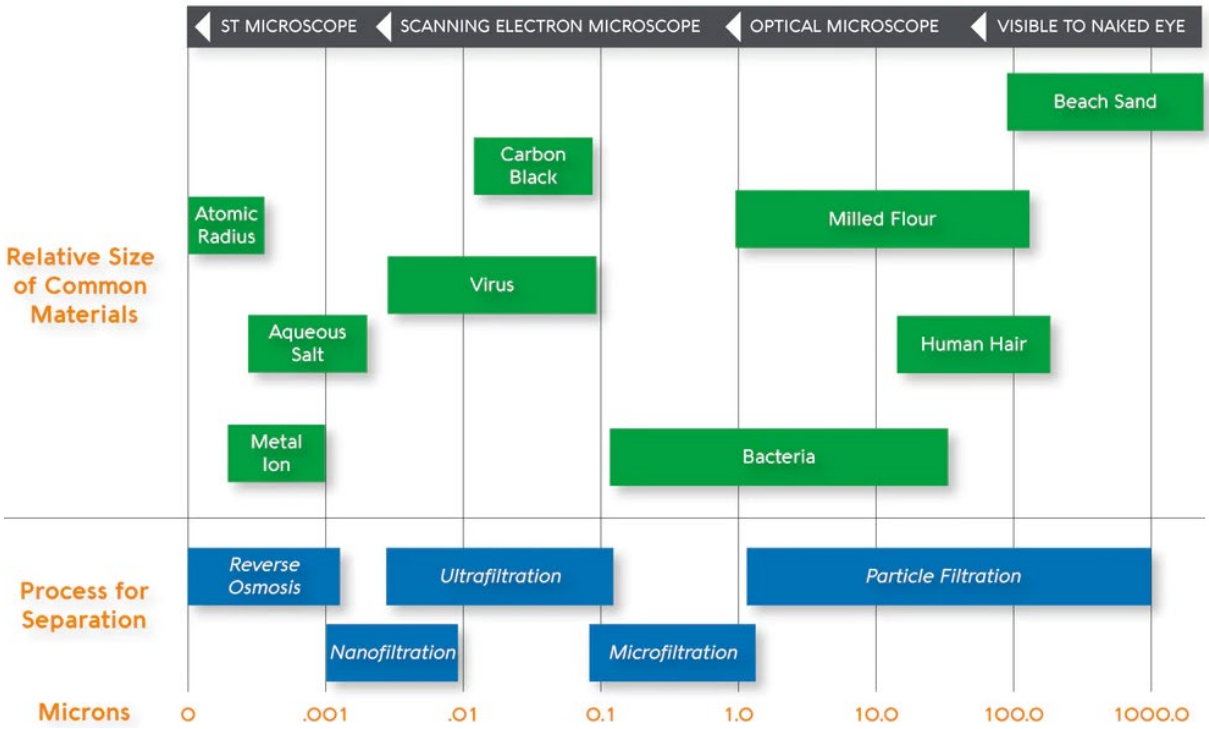

Figure I.11 Overall Filtration Spectrum [31]

I.4. Membrane Supports

I.4.1. Membrane Supports Definition

Membrane supports are essential components in membrane separation processes, providing structural integrity to the membrane and facilitating efficient separation of substances.

Membrane supports are materials that provide mechanical strength and structural integrity to the thin, semi-permeable membranes used in separation processes. They help prevent the membrane from collapsing under pressure and maintain its separation efficiency.

when composed of ceramics, serve as the foundational structure upon which the semi-permeable membrane is deposited or integrated, as shown in Figure I.12. Ceramics are widely used as support materials due to their excellent mechanical strength, chemical resistance, and thermal stability.

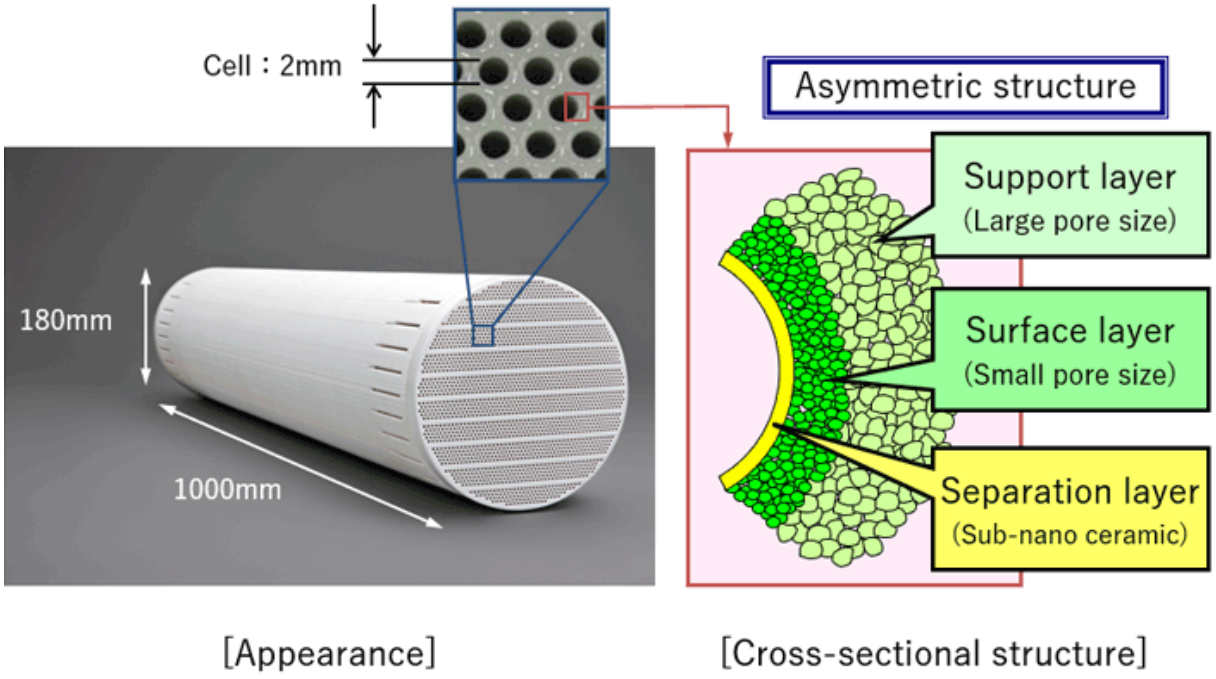

Figure I.12 ceramic membrane support and a diagram of cross section [32]

I.4.2. Membrane Supports Configurations

Membrane supports come in various configurations to suit different separation processes and applications. Some common configurations include:

I.4.2.1. Flat Configuration

Noted as one of the simplest and earliest forms, consist of a thin, flat layer or a group of layers, typically supported by materials such as ceramics, metals, or polymers, as depicted in Figure I.13, this configuration, where the membrane is sustained by a flat surface, is frequently employed in applications where the feed solution flows parallel to the membrane surface, facilitating efficient separation processes.[14]

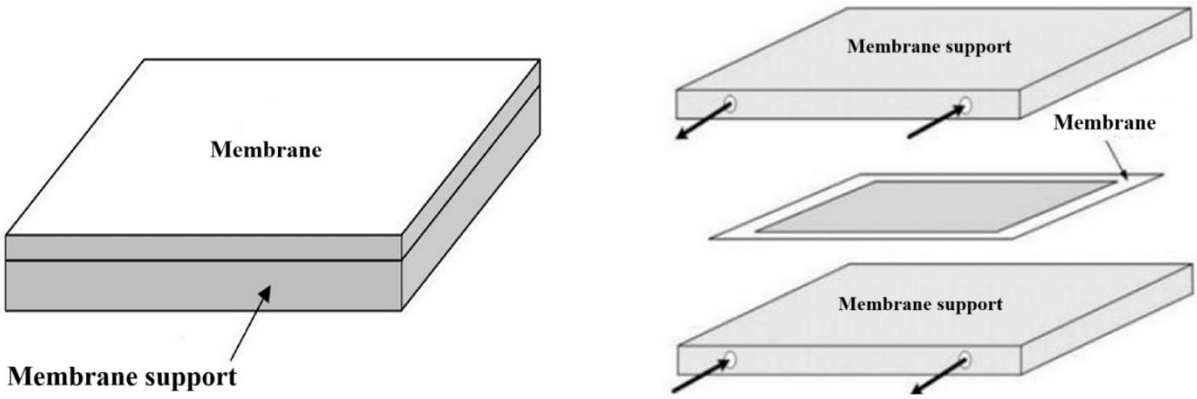

Figure I.13 Flat Membrane Configuration Illustration [33]

I.4.2.2. Tubular Configuration

In the tubular configuration, the membrane is wrapped around a tubular support structure, such as a porous ceramic. This configuration is well-suited for applications where high pressures or temperatures are involved, and it allows for efficient separation in a compact design. The fact that filtered water leaves through the sides of the tube, facilitated by micro-perforations, enhances overall filtration effectiveness. Additionally, it may be single-channel, as in Figure I.14 (right), or multi-channel (left), as in Figure I.14, providing versatility in design to meet specific operational requirements. [14]

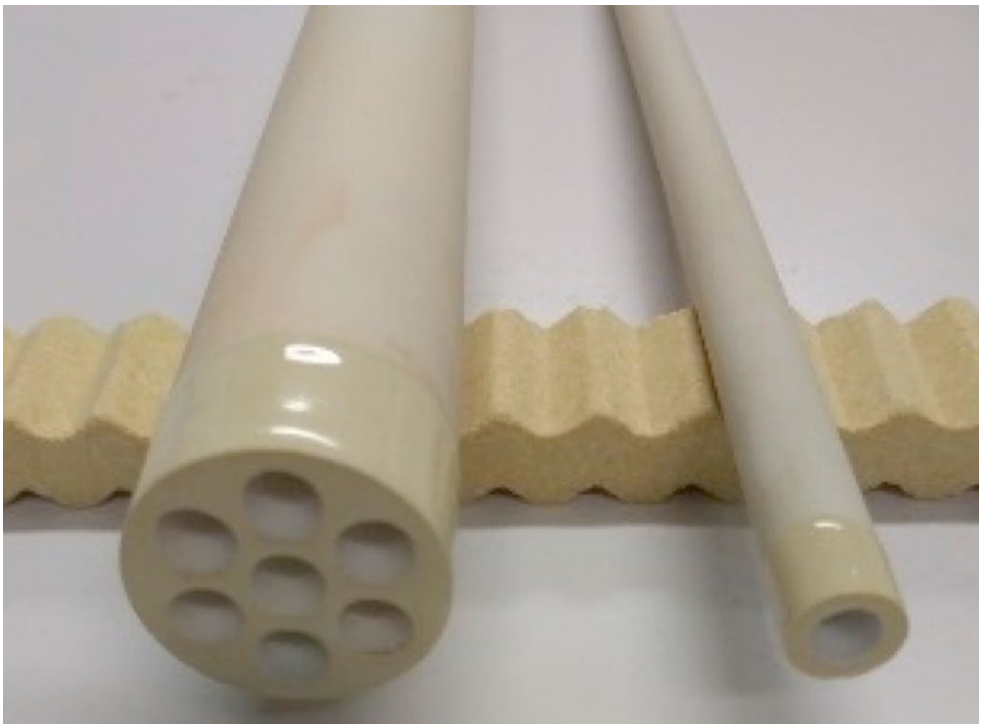

Figure I.14 Tubular ceramic multi-channel (left) and single-channel (right) prepared at CTI. [34]

I.4.2.3. Hollow-Fiber

Hollow-fiber membranes consist of many small, hollow fibers bundled together. These fibers serve as both the membrane and the support structure, providing a large surface area for separation in a compact design. This configuration is commonly used in applications such as water purification and blood dialysis, hollow fiber usually has a membrane coated on the

outside of a porous fiber support as shown in Figure I.16 Hollow fiber modules are characteristically 10–20 cm in diameter and 1.0–1.6 m long. [15]

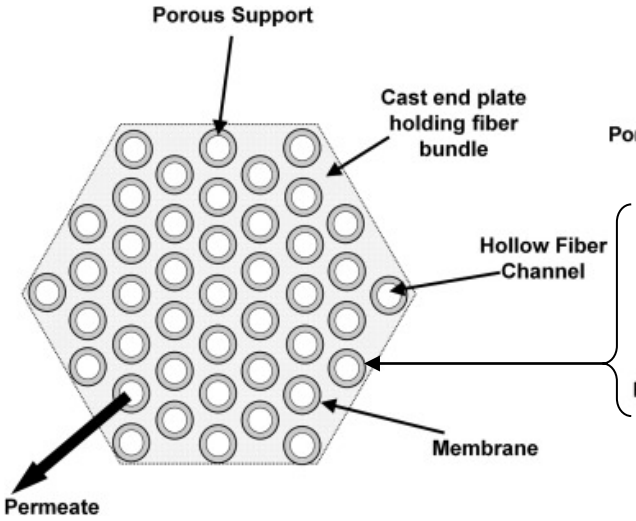

Figure I.16 Schematic of a hollow fiber bundle used in gas separation. [15]

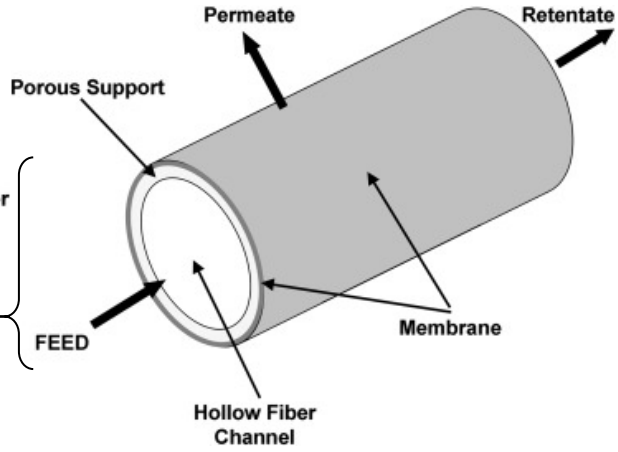

Figure I.15 Schematic of a hollow fiber used in gas separation. [15]

I.4.2.4. Spiral Wound

Spiral wound membranes consist of a membrane sheet wound around a permeate tube, with feed spacers placed between the membrane layers. This configuration maximizes the surface area available for separation while maintaining structural integrity and allowing for efficient fluid flow. Spiral wound membranes are widely used in various industrial applications, including desalination and wastewater treatment.

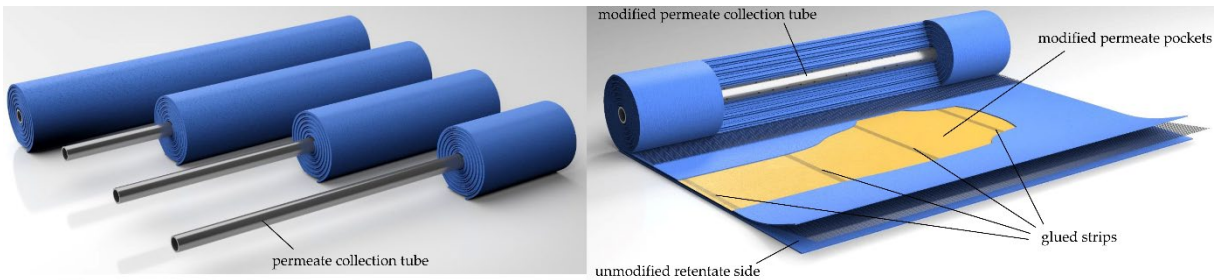

Figure I.17 Graphical illustration of Spiral Wound membrane [35]

I.4.3. Membrane Supports Manufacturing Methods

The preparation of a ceramic membrane support normally involves the following steps: (1) forming particle suspensions; (2) packing the particles in the suspensions into a membrane precursor with a certain shape using various shaping techniques such as slip casting, tape casting, extrusion, and pressing; and (3) sintering the membrane precursor at elevated temperature.

I.4.3.1. Extrusion Method

Extrusion is a common method for producing bodies in the ceramic industry with the advantages of high production efficiency and good product uniformity [16]. However, the

extrusion process places high demands on slurry materials, requiring the slurry to have sufficient plasticity, fluidity, and uniformity; otherwise, the billet is prone to torsional deformation and cracking. The extrusion process consists of five steps: mixing, extrusion, compression, cutting, drying, and sintering. During the extrusion process, the ceramic powder is mixed with surfactants, anticoagulants, plasticizers, and additives, stirred, stored for several hours at room temperature and high humidity, and then injected into a chamber where it is compressed. The inside of the chamber has a die opening with a piston that exerts a force on the slurry. The shape, pore size distribution, and porosity of the final product are determined by the applied force (typically 20–180 MPa). The film is then cut to the desired length, dried, and sintered to prevent cracking and bending. There are two types of extruders to be mentioned here—screw and plunger extruders. The use of a plunger extruder can reduce the possibility of contamination due to wear; however, there is a significant pressure loss that affects the die pressure; the plunger and the die pressure of the screw extruder are similar to that of the plunger. [10]

I.4.3.2. Pressing Method

In the pressing method, the powder is granulated with a small amount of binder, and the resulting granulated powder is placed in a mold and compacted directly with a press machine. Dry and isostatic pressing are widely used techniques in pressing processes [17]. In the dry-pressing process, particles extrude from each other, creating internal friction that binds the powder particles more closely. The technological steps include feeding, compression, molding, billet production, mold cleaning, and it involves relatively simple operations. Due to its straightforward process, this method is commonly employed for producing substrate products such as plate ceramic films. As the industry seeks economically competitive membranes, alongside exploring alternative low-cost ceramic materials and reducing sintering temperatures, pressing emerges as an environmentally friendly and cost-effective alternative. [10]

I.4.3.3. Slip-Casting Method

It is well established that slip casting is a suitable and well-established technique for preparing ceramic samples with complex shape and high homogeneity [18], [19]. In the slip-casting technique a slip, or aqueous suspension of solid particles, is poured into a porous mold, usually made of plaster of Paris. Water from the slip is absorbed by the mold, leading to the formation of a solid layer on the mold walls. The thickness of this solid layer is related to the time in which the slip is kept in the mold. The excess of water is subsequently removed from the mold in a drying procedure. The obtained green body is then sintered. The sintering temperature will depend on the composition and desired properties of the finished piece. [18]

Chapter II: Raw Material Analysis

II.1. Raw Materials

Kaolin was selected as the raw material for fabricating the tubular supports due to its high alumina content, as indicated in Table II.8, which confers upon it a significant mechanical strength. Furthermore, its abundant presence in nature and accessibility through modern excavation techniques make it a locally available resource of considerable value.

The kaolin utilized in this study was procured from the Jebel Debagh mine in Roknia, Guelma, a fact illustrated in Figures II.1 and II.2.

II.1.1. Location

The mine is situated at the Google Maps address of G7M6+C64, Roknia. With coordinates of 36°32'00.7"N 7°15'38.0"E. It is located approximately 32.9 km west of Guelma city.

Figure II.1 Satellite image of "Mine of Jebel Debagh"

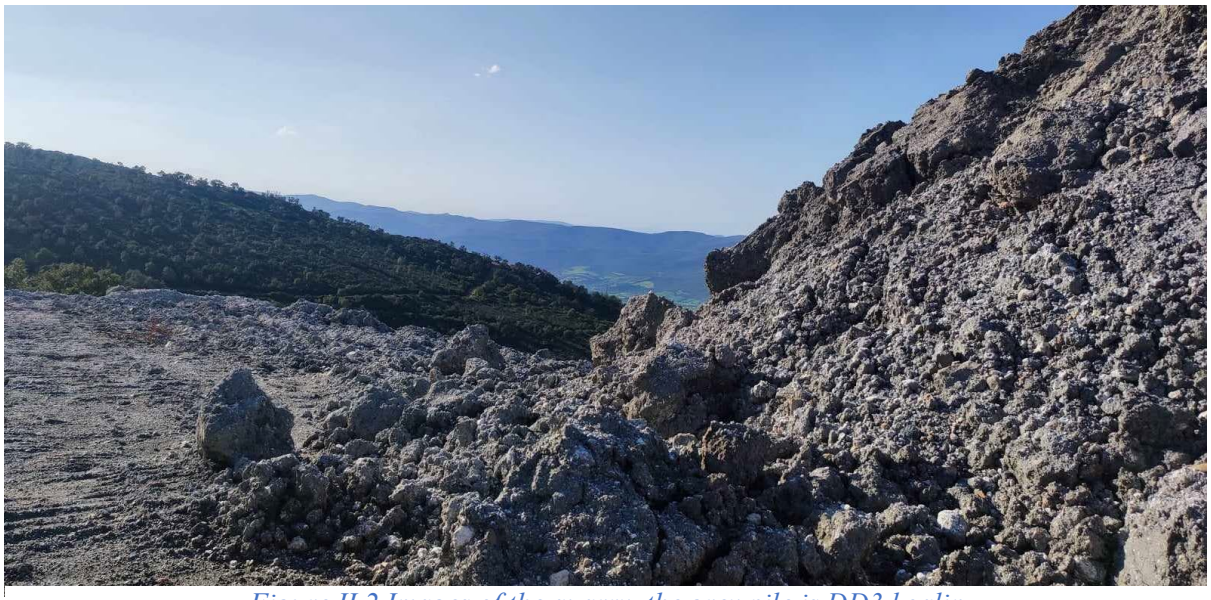

Figure II.2 Images of the quarry, the grey pile is DD3 koalin

II.1.2. Preparations of The Rock Samples

Two primary samples were obtained from the quarry: DD3 kaolin, distinguished by its dark gray color with white spots, as depicted in the Figure II.3, and a second sample consisting of rocks containing a blend of DD1 and DD2 kaolin. This mixture is characterized by a distinctive white appearance with streaks of red, indicative of impurities such as Fe_2O_3, as shown in the Figure II.4. The initial preparation process for the DD1 samples involves initially cleaning the exterior of the rocks to remove dirt and other contaminants. Subsequently, the rocks are broken into smaller fragments, and they are sorted based on color, with those exhibiting the fewest to no red streaks designated as DD1 due to their lower impurity content.

Figure II.3 DD3 Kaolin sample

Figure II.4 DD1 rocks before and after cleaning

II.1.3. Grinding

The grinding process involves initially manually grinding the rocks with hand tools to reduce their size and prepare them for further processing. Subsequently, the RETSCH Jaw Crusher BB1 is utilized to further grind the rocks to the desired fineness. This machine ensures consistent particle size reduction and is capable of producing uniform results.

Figure II.5 The RETSCH Jaw Crusher; Type: BB1 A

II.1.4. Calcination

The kaolin underwent a calcination process, the process involved loading the kaolin (DD1 and DD3) into a kiln and heating it to 600°C. The kiln was maintained at this temperature for one hours to ensure thorough calcination. During this time, the kaolin underwent chemical changes, losing water and breaking down its structure to form metakaolin. This transformation is crucial as it removes impurities and enhances the material's suitability, Graph II.1 illustrates the heating process, with a heating rate of $5\ °C/min$.

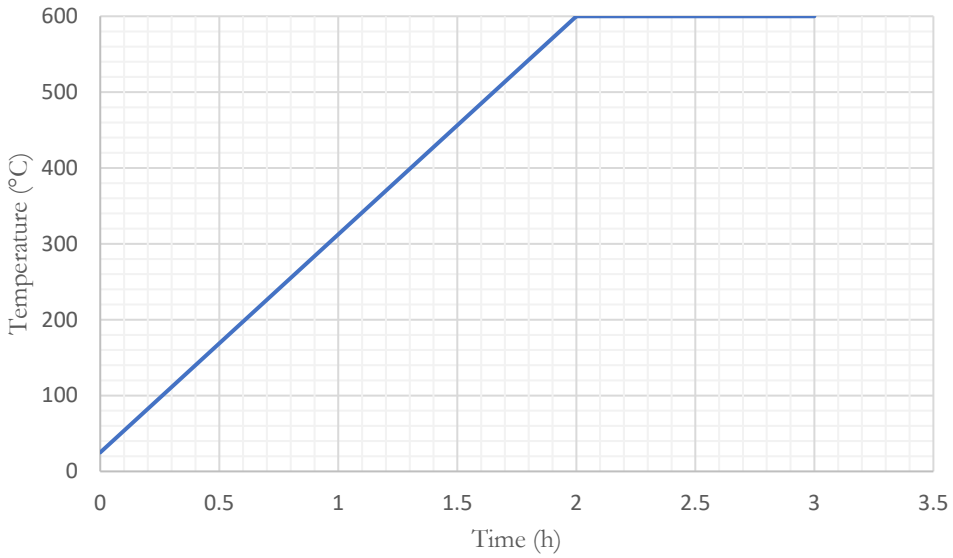

Graph II.1 Plot illustrating the heating process within the kiln

II.1.5. Sieving

Following the grinding process with the Jaw Crusher, we proceeded to sieve the material using the Retsch Horizontal Sieve Shaker AS 200 Control, as depicted in Figure II.6. This equipment ensures precise and uniform sieving of particles. A $200\,\mu m$ sieve mesh was employed to determine the grain size.

Figure II.6 Retsch Horizontal Sieve Shaker AS 200 Control

Resulting in particles of $200\,\mu m$ or smaller being retained. This step is crucial for ensuring consistency in particle size distribution, which is essential for subsequent analyses and experiments. Following sieving, we prepared multiple samples, each weighing approximately 40 grams, for chemical analysis, as depicted in Figure II.7. This meticulous preparation ensures representative sampling and accurate assessment of the material's chemical composition.

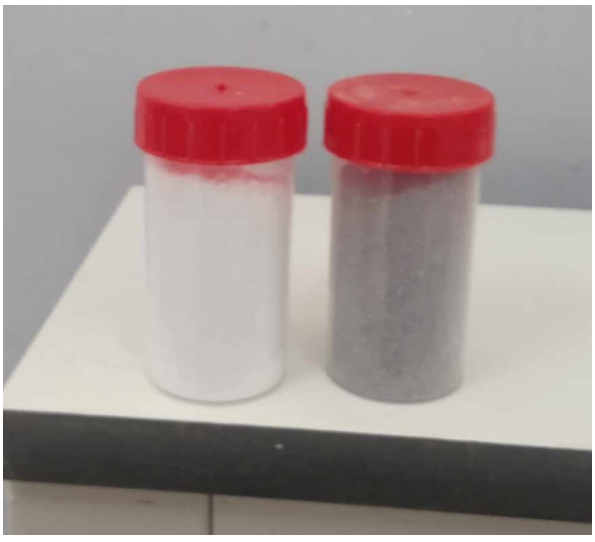

Figure II.7 DD1 & DD3 samples prepared for chemical analysis

II.2. Chemical Analysis

Chemical analysis plays a crucial role in understanding the composition and properties of materials. Various analytical techniques are employed for this purpose, in this section, we delve into several key methods utilized in the comprehensive analysis of the kaolin sample.

II.2.1. FTIR Analysis

Fourier Transform Infrared (FTIR) spectroscopy is an analytical technique widely used for probing the molecular structure and chemical bonds present within a sample. By measuring the absorption and transmission of infrared light across a range of wavelengths, FTIR spectroscopy provides detailed information on the functional groups and molecular composition of the sample. This technique is particularly valuable for identifying and quantifying different molecular species and understanding their interactions within complex matrices. In this study, we employed the PerkinElmer Spectrum Two™ IR spectrometer, which offers high sensitivity and resolution, to acquire and analyze the infrared spectra. The resulting spectra, as depicted in Graphs II.2 to II.5, reveal critical insights into the molecular architecture of the DD1 and DD3 samples.

Figure II.8 PerkinElmer Spectrum Two™ IR Spectrometer

The data collected from the IR spectrometer was then exported as an Excel file. We used Origin 2018 to plot the graphs.

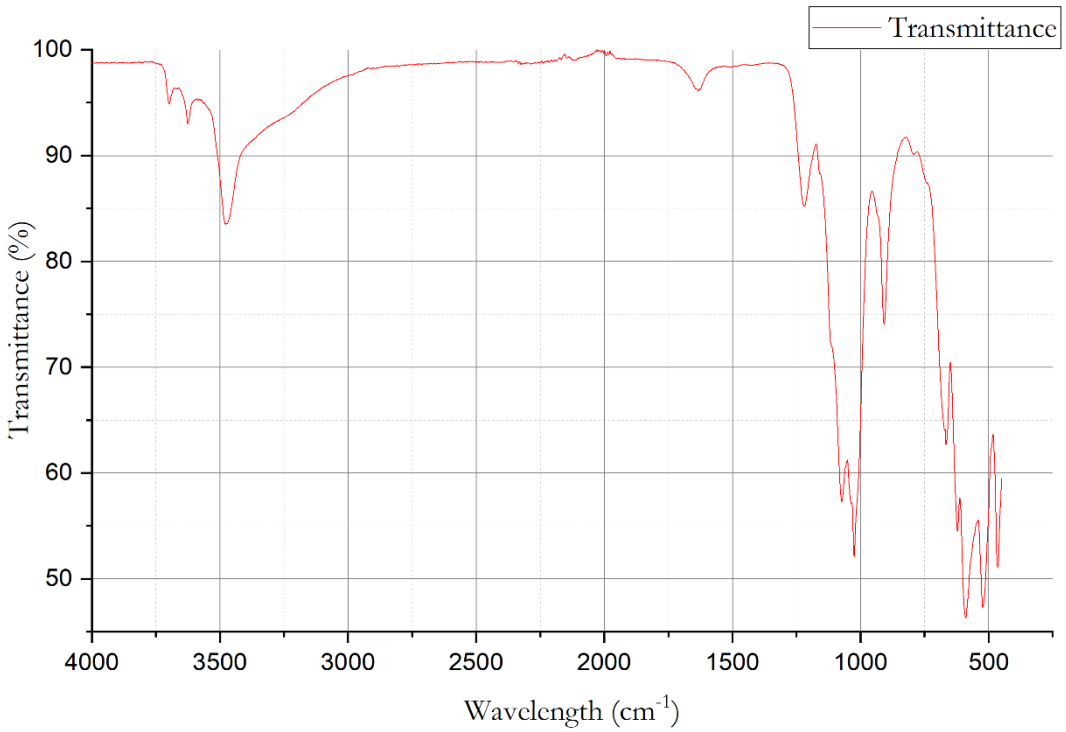

Graph II.2 FTIR spectrum of DD1 before calcination

Table II.1 Peak values (cm^{-1}) and corresponding Transmission (%) observed for DD1 sample before calcination

Wavelength cm^{-1}	3699	3626	3479	1644	1222	1074	1025	907	667	623	594	523
Transmission %	94.87	93.02	83.53	96.32	85.29	57.3	52.06	74.06	62.74	54.6	46.76	47.39

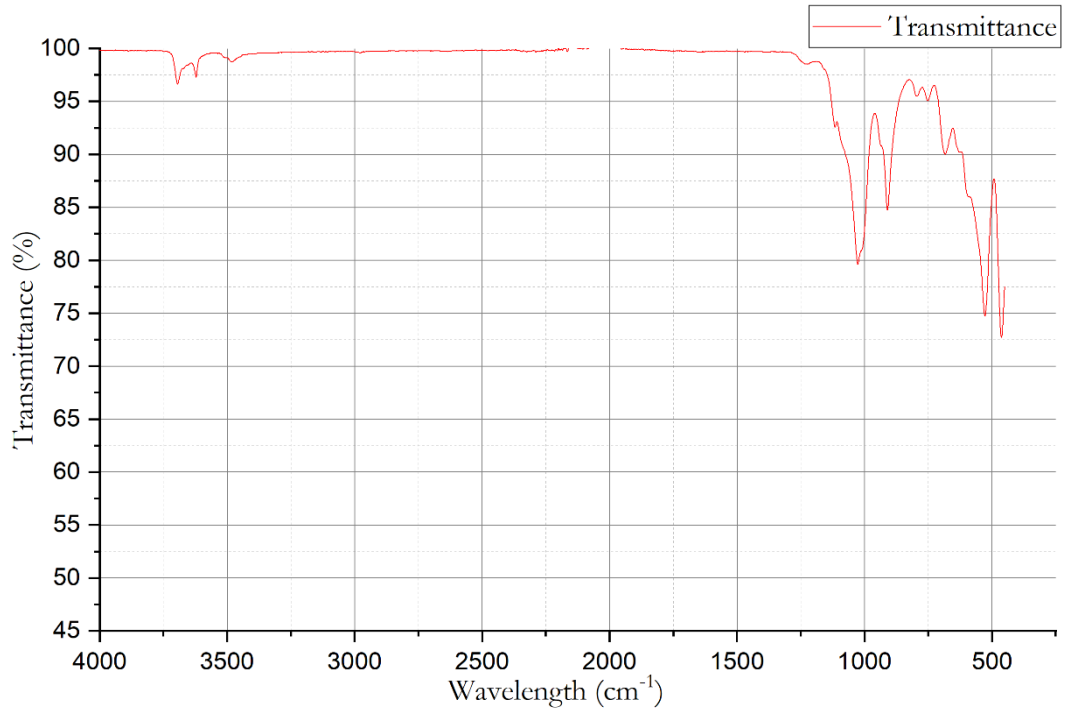

Graph II.3 FTIR spectrum of DD1 after calcination at 600 °C

Table II.2 Peak values (cm^{-1}) and corresponding Transmission (%) observed for DD1 sample after calcination at 600 °C

Wavelength cm^{-1}	3694	3622	3485	1118	1025	907	684	528	464
Transmission %	96.66	97.31	98.74	92.72	79.67	85.17	90.03	74.73	72.8

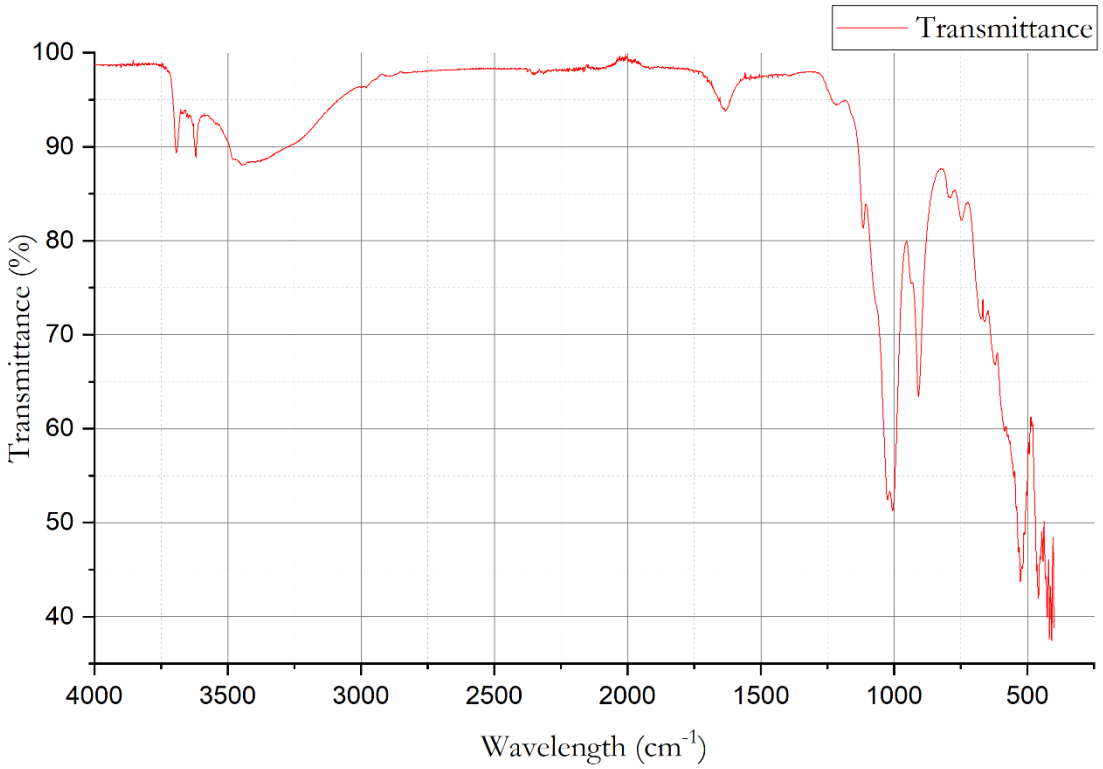

Graph II.4 FTIR spectrum of DD3 before calcination

Table II.3 Peak values (cm^{-1}) and corresponding Transmission (%) observed for DD3 sample before calcination

Wavelength cm^{-1}	3693	3620	3446	1634	1120	1002	908	526	460
Transmission %	89.39	88.9	88.01	93.8	82.15	52.04	63.52	43.74	42.13

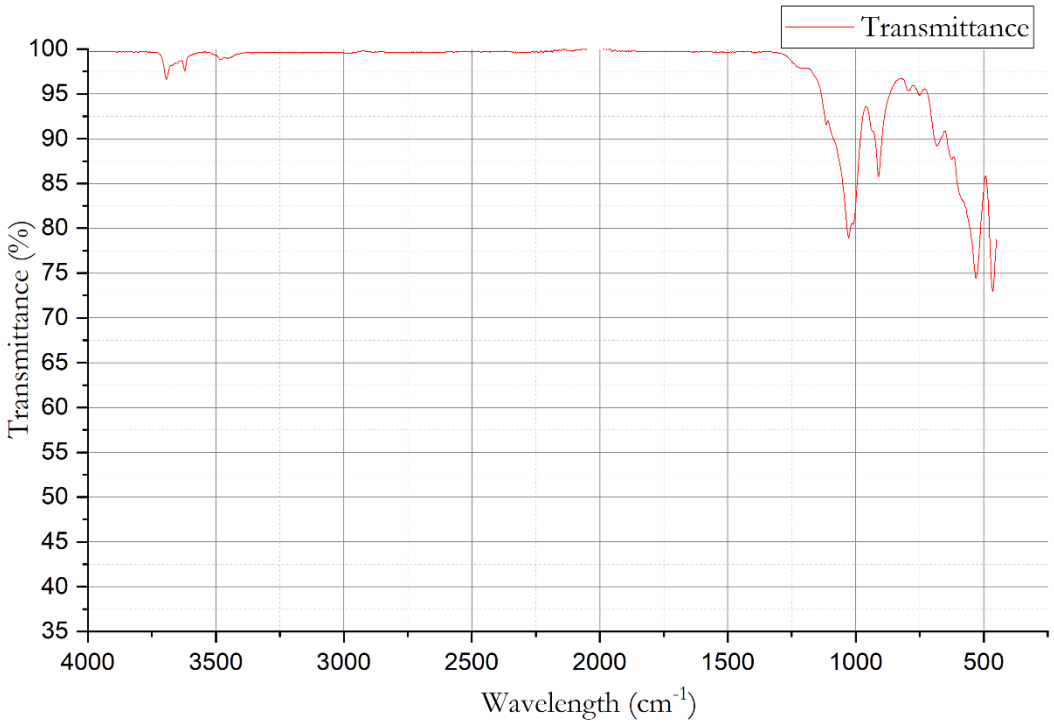

Graph II.5 FTIR spectrum of DD1 after calcination at 600 °C

Table II.4 Peak values (cm^{-1}) and corresponding Transmission (%) observed for DD3 sample after calcination at 600 °C

Wavelength cm^{-1}	3694	3621	3451	1028	911	683	531	465
Transmission %	96.64	97.55	98.99	78.92	85.76	89.22	74.44	72.97

After reviewing the relevant literature, we can summarize the results in Table II-5, describing peak values and corresponding groupings observed for the DD1 & DD3 before and after calcination, along with their assignments.

Table II.5 Peak values and corresponding groupings assignments observed for the DD1 & DD3 [19]

DD1 cm^{-1}	*DD1 at 600 °C cm^{-1}*	*DD3 cm^{-1}*	*DD3 at 600 °C cm^{-1}*	*Assignments*
3699	3694	3693	3694	*Hydroxyl O-H stretching vibration*
3626	3622	3620	3621	*Hydroxyl O-H stretching vibration*
3479	3485	3446	3451	*Hydroxyl O-H stretching vibration*
1644	---	1634	---	*H–O–H bending band of water*
1222	1118	1120	---	*Si-O-Si stretching of kaolin*
1025	1025	1002	1028	*Si-O-Si stretching of kaolin*
907	907	908	911	*Al-OH bonds of kaolinite.*
667	684	---	683	*Si-O & Si-O-Al vibrations*
594	---	---	---	*N/A*
523	528	526	531	*Si-O & Si-O-Al vibrations*
---	464	460	465	*Si-O bending vibrations*

Table II.6 Transmission Values for DD1 Kaolin Before and After Calcination

Peak Wavenumber cm^{-1}	Transmission Before Calcination (%)	Transmission After Calcination (%)	Change in Transmission (%)
3699	94.87	96.66	+1.79
3626	93.02	97.31	+4.29
3479	83.53	98.74	+15.21
1644	96.32	100	+3.68
1222	85.29	92.72	+7.43
1025	52.06	79.67	+27.61
907	74.06	85.17	+11.11
667	62.74	90.03	+27.29
523	47.39	74.73	+27.34

The transmission values for the hydroxyl (-OH) stretching vibrations at 3699 cm^{-1}, 3626 cm^{-1}, and 3479 cm^{-1} significantly increased after calcination, indicating a reduction in the absorption of these functional groups. This suggests that the calcination process led to a reduction in the presence of hydroxyl groups in the DD1 kaolin sample.

Interestingly, the transmission at 1644 cm^{-1}, corresponding to water bending vibrations, increased after calcination to 100 %. This could indicate the removal or reduction of water molecules in the sample due to the heating process.

Additionally, the transmission values for peaks associated with Si-O and Al-O stretching and bending vibrations (1122 cm^{-1}, 1025 cm^{-1}, 907 cm^{-1}, 667 cm^{-1}, 523 cm^{-1}) showed varying degrees of change after calcination. These changes may reflect alterations in the molecular structure and composition of the kaolin sample as a result of calcination.

Table II.7 Transmission Values for DD3 Kaolin Before and After Calcination

Peak Wavenumber cm^{-1}	Transmission Before Calcination (%)	Transmission After Calcination (%)	Change in Transmission (%)
3693	89.39	96.64	+7.25
3620	88.9	97.55	+8.65
3446	88.01	98.99	+10.98
1634	93.8	100	+6.2
1002	52.04	78.92	+26.88
908	63.52	85.76	+22.24
526	43.74	74.44	+30.7
460	42.13	72.97	+30.84

The transmission values for the hydroxyl (-OH) stretching vibrations at 3693 cm^{-1}, 3620 cm^{-1}, and 3446 cm^{-1} significantly increased after calcination, indicating a reduction in the absorption of these functional groups. This suggests that the calcination process led to a reduction in the presence of hydroxyl groups in the DD1 kaolin sample.

Interestingly, the transmission at 1634 cm^{-1}, corresponding to water bending vibrations, increased after calcination to 100 %. This could indicate the removal or reduction of water molecules in the sample due to the heating process.

Additionally, the transmission values for peaks associated with Si-O and Al-O stretching and bending vibrations (1002 cm^{-1}, 908 cm^{-1}, 526 cm^{-1}, 460 cm^{-1}) showed varying degrees of change after calcination. These changes may reflect alterations in the molecular structure and composition of the kaolin sample as a result of calcination.

II.2.2. TGA/DSC Analysis

Thermogravimetric Analysis (TGA) and Differential Scanning Calorimetry (DSC) are thermal analysis techniques used to study the physical and chemical properties of materials as a function of temperature. TGA measures changes in weight as a sample is heated, while DSC measures changes in heat flow, allowing for the determination of phase transitions, decomposition temperatures, and other thermal properties, we employed the LABSYS evo TGA STA DTA/DSC by Setaram, capable of reaching temperatures up to 1600°C, to get Graphs II.6 and II.7. The device is depicted in Figure II.9.

Figure II.9 LABSYS evo Device by Setaram

The initial mass and temperature of sample DD1 were 414 mg and 25°C, respectively. Over the course of approximately 128 minutes, the temperature gradually increased to 1186°C at an average heating rate of 9°C/min. The results are illustrated in graph II-6.

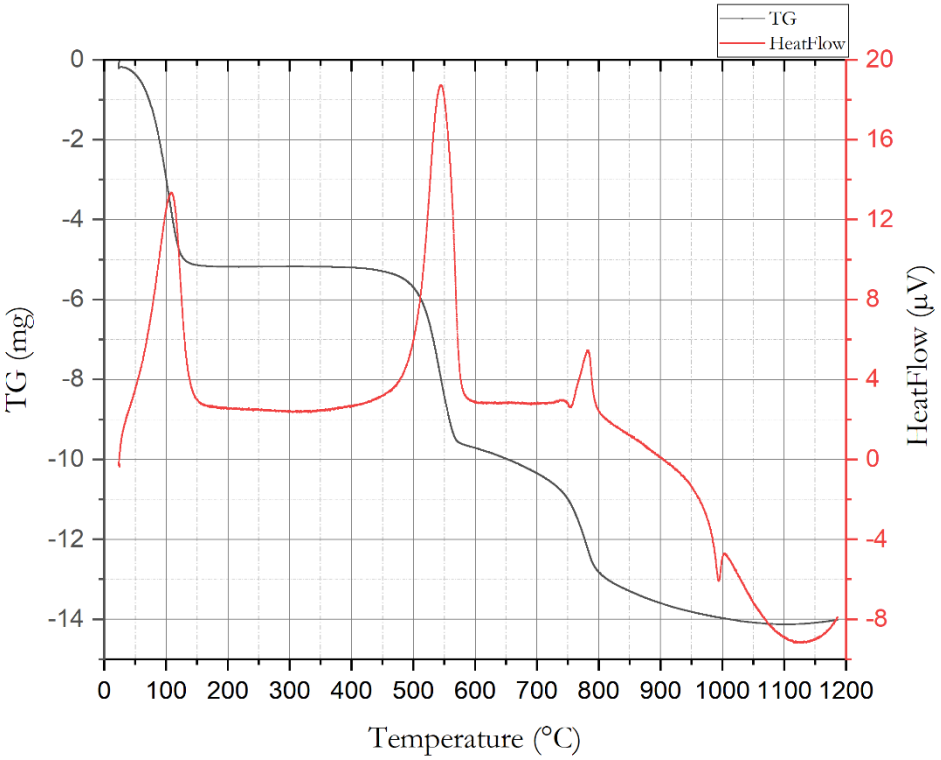

Graph II.6 Thermogravimetric Analysis and Differential Scanning Calorimetry Curve for DD1

For the DD1 sample, we observe the following thermal transformations:

- Three exothermic transformations at approximately 108°C, 545°C, and 782°C.
- Two endothermic transformations at approximately 755°C and 994°C."

Regarding the mass loss, we observe four distinct stages of mass decline as the temperature increases:

- From 25°C to 130°C:

  This range corresponds to the loss of adsorbed water, indicated by an exothermic peak at 108°C.

- From 460°C to 565°C:

  This range involve the decomposition of certain organic compounds or, reflected by an exothermic peak at 545°C.

- From 565°C to 790°C:

  This stage could involve further evaporation of water inside the Kaolinite phase.

- From 790°C to 1020°C:

  This range might be associated with the breakdown of the most thermally stable components or the formation of new phases probably mullite that result in the release of gaseous products, also shown by distinct endothermic peak in the DSC curve at 994°C.

The initial mass and temperature of sample DD3 were 42.3 mg and 25°C, respectively. Over the course of approximately 128 minutes, the temperature gradually increased to 1186°C at an average heating rate of 9°C/min. The results are illustrated in Graph II-7

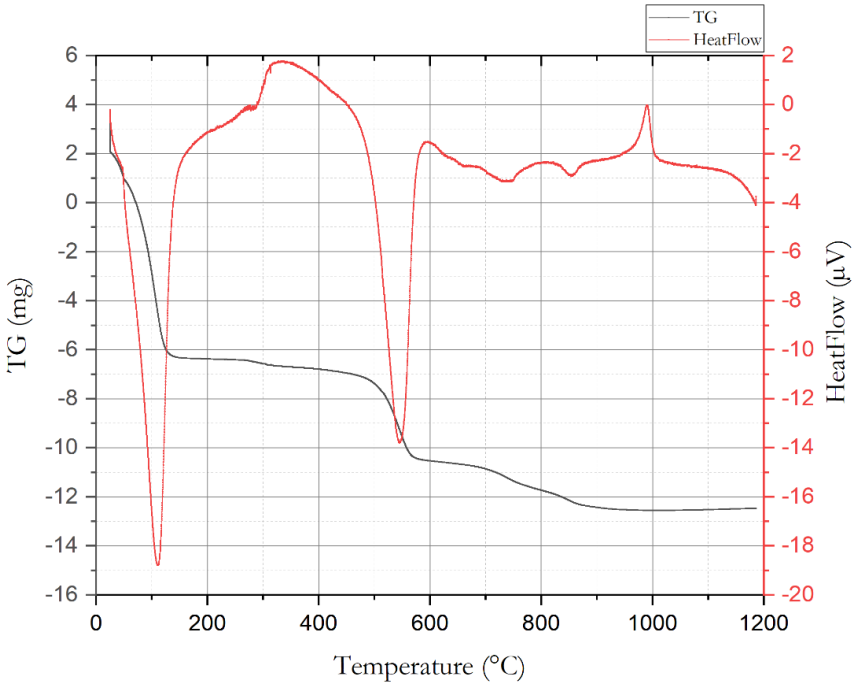

Graph II.7 Thermogravimetric Analysis and Differential Scanning Calorimetry Curve for DD3

For the DD3 sample, we observe the following thermal transformations:

- One exothermic transformation is observed at approximately 991°C.
- Four endothermic transformations occur at approximately 112°C, 545°C, 747°C, and 854°C.

Regarding the mass loss, we observe three distinct stages of mass decline as the temperature increases:

- From 25°C to 125°C:

  The mass loss observed between 25°C and 125°C likely corresponds to the desorption of adsorbed water. This stage is characterized by an initial decline in mass, indicating the removal of low-boiling-point volatiles and moisture.

- From 480°C to 580°C:

  This stage suggests a significant thermal event involving the decomposition or volatilization of organic components within the sample.

- From 700°C to 875°C:

  This stage signifies a further decomposition or transformation within the sample. This temperature range may involve the decomposition of more thermally stable components or the formation of new phases such as mullite that result in the release of gaseous products

As for the endothermic and exothermic peaks, endothermic transformations indicate that the sample absorbs heat from the environment, resulting in the movement of atoms or particles away from each other. Conversely, exothermic transformations release heat to the environment, causing atoms or particles to move closer together. Each thermal event corresponds to a reduction in sample mass.

The transformation occurring around 100°C is typically associated with the loss of water from the material. Other thermal events are linked to structural transformations, reorganization of atomic or molecular bonds, or the loss of hydroxyl groups from the structure.

To further clarify these transformations, we can revisit the FTIR spectroscopy used and the upcoming XRD analyses. FTIR reveals chemical bonds affected during thermal events, while XRD identifies new crystalline structures. These techniques offer insight into thermal behaviors in DD1 and DD3. Subsequent sections present XRD patterns, correlated with DSC data for interpretation.

II.2.3. X-Ray Fluorescence Analysis

X-Ray Fluorescence (XRF) analysis is a non-destructive technique used to determine the elemental composition of materials. By bombarding a sample with X-rays, it emits characteristic fluorescent X-rays, which are then measured to identify and quantify the elements present. We employed the Zetium XRF spectrometer from Malvern PANalytical.

Figure II.10 The Zetium XRF Spectrometer

Table II.8 Results of Percentage Oxides from XRF Analysis

Composition	SiO_2	Al_3O_2	Fe_2O_3	CaO	MgO	SO_3	K_2O	Na_2O
DD1 (wt%)	*45.02*	*39.25*	*0.06*	*0.03*	*0.07*	*2.2*	*0.41*	*0*
DD3 (wt%)	*38.8*	*36.18*	*0.12*	*0.04*	*0.1*	*7.09*	*0.97*	*0*

- SiO_2 content: DD1 has a higher SiO_2 content (45.02 wt%) compared to DD3 (38.8 wt%), indicating that DD1 has a higher proportion of silica in its composition.
- Al_3O_2 content: DD1 also has a higher Al_3O_2 content (39.25 wt%) compared to DD3 (36.18 wt%), suggesting a higher proportion of alumina in DD1.
- Fe_2O_3 content: Both samples have very low iron oxide content, with DD1 at 0.06 wt% and DD3 at 0.12 wt%.
- As for the rest of the elements such as CaO, MgO, K_2O Both samples have very low Content with impurities, one notable exception is SO_3 at 2.2 wt% and 7.09 wt%.

II.2.4. X-Ray Diffraction Analysis

X-Ray Diffraction (XRD) analysis is a powerful tool for determining the crystal structure and phase composition of materials. X-rays are directed at a crystalline sample, and the resulting diffraction pattern provides information about the arrangement of atoms within the material. For this analysis we used CubiX^3 X-ray diffractometers from Malvern Panalytical.

Figure II.11 CubiX^3 X-ray Diffractometers

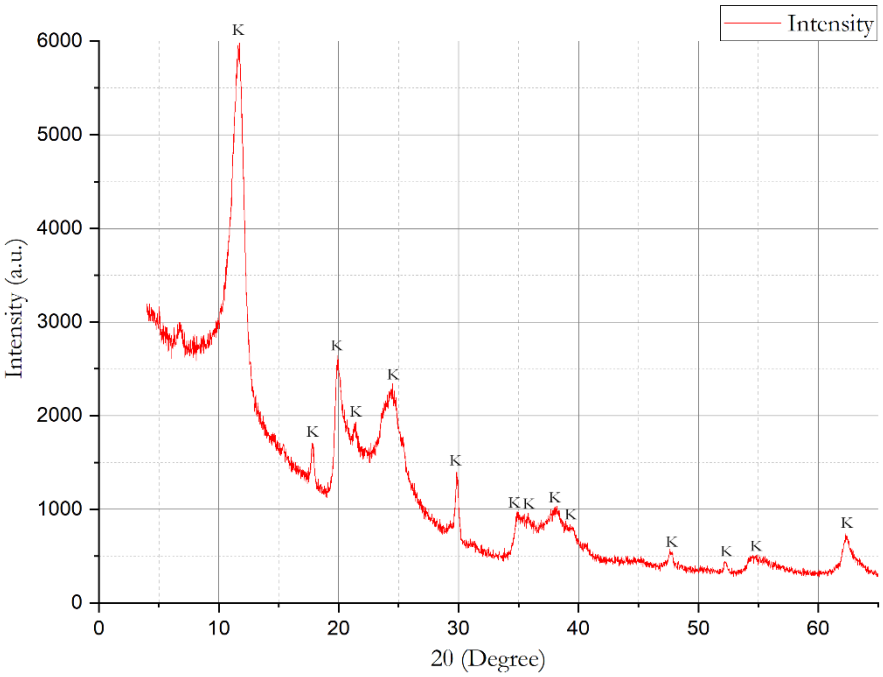

Graph II.8 XRD Spectra of DD1 sample. K: Kaolinite 1A

Using HighScore Plus software to analyze Graph II.8 revealed that the peaks correspond to Kaolinite 1A. The chemical formula of Kaolinite 1A is $H_4Al_2O_9Si_2$, and its reference code is 98-006-8698.

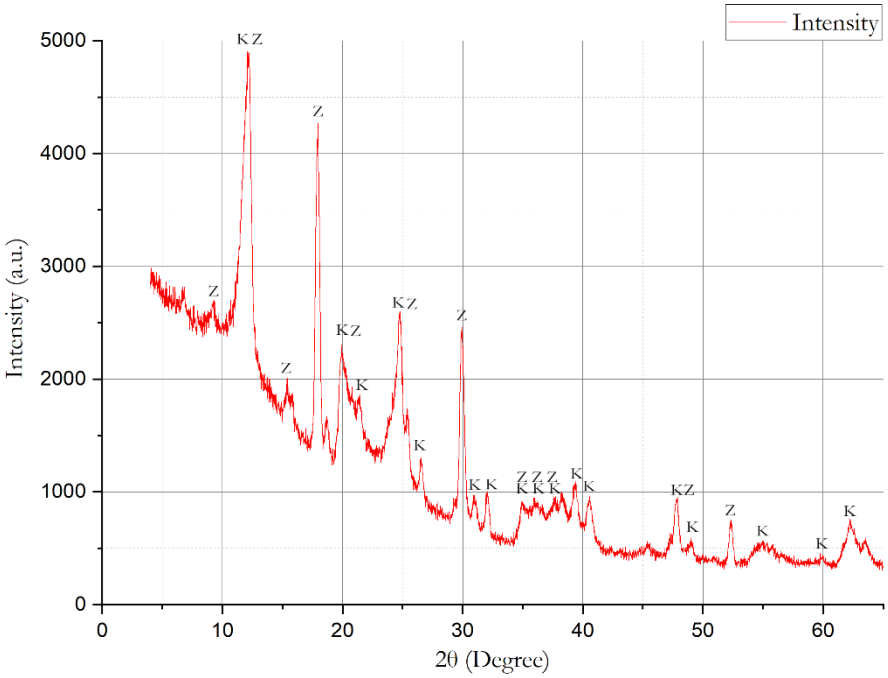

Graph II.9 XRD Spectra of DD3 sample

Using HighScore Plus software to analyze Graph II.9 revealed that most of the peaks correspond to Kaolinite 1A. The chemical formula of Kaolinite 1A is $H_4Al_2O_9Si_2$, and its reference code is 98-006-8698. The remaining peaks likely correspond to Zeolite (calcined) with the chemical formula O_2Si_1 and the reference code 98-017-3142.

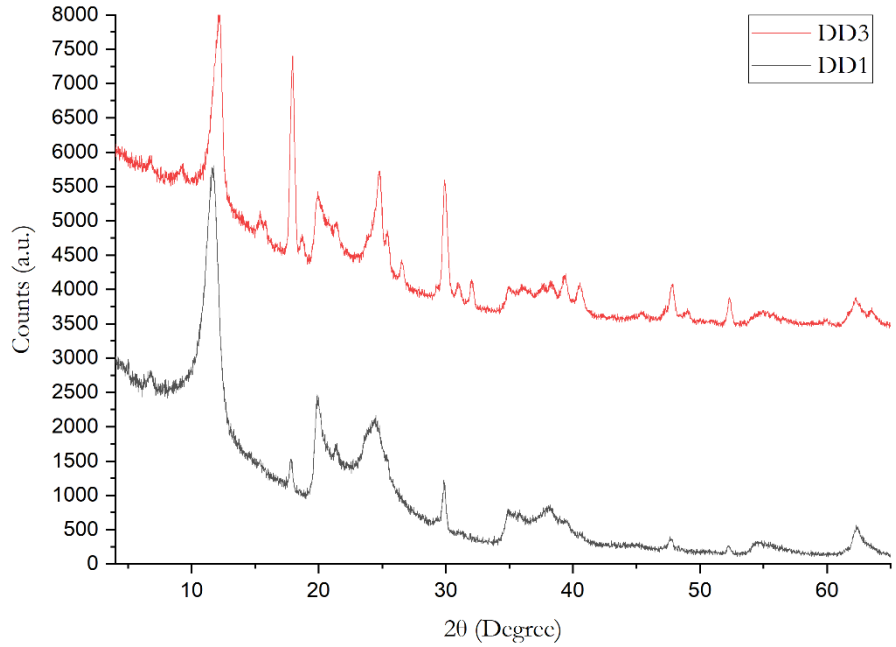

Graph II.10 XRD Comparison Between DD1 and DD3

We notice from Graph II.10 that the sample DD1 exhibits stronger intensity peaks compared to sample DD3. This suggests that DD1 has a higher concentration of kaolinite. In XRD analysis, a higher kaolinite phase concentration means a larger proportion of the X-rays are diffracted by the kaolinite crystal structure, resulting in stronger peaks. Therefore, the stronger peaks in DD1 indicate a higher relative abundance or purity of kaolinite in this sample, while the weaker peaks in DD3 suggest a lower concentration of kaolinite or the presence of additional phases that dilute its diffraction signal.

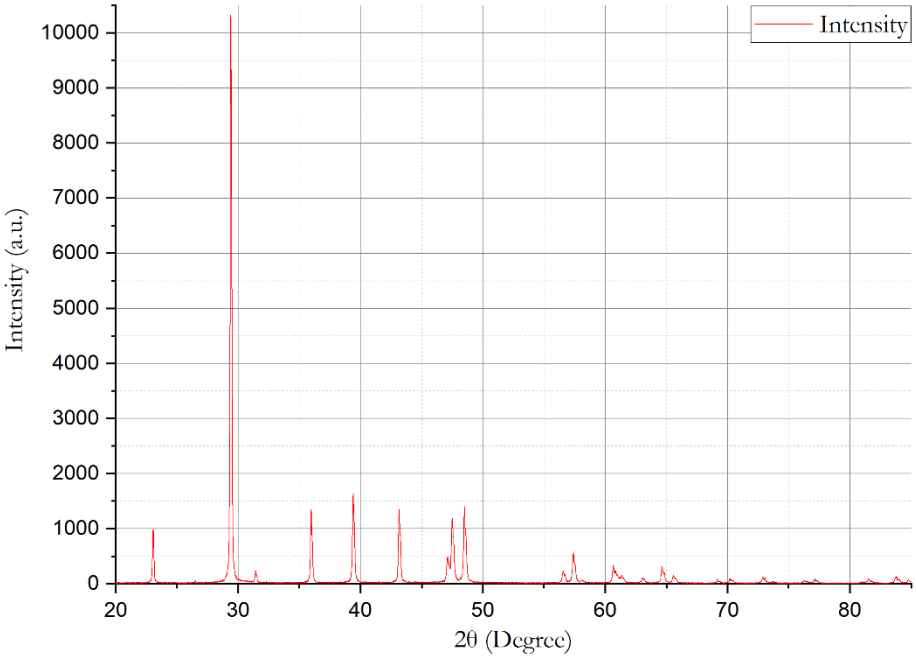

Graph II.11 XRD Spectra of Calcite sample

Using HighScore Plus to analyze the Graph II.11 revealed that the peaks correspond to Calcite. The chemical formula of Calcite is $Ca_6C_6O_{18}$, and its reference code is 96-901-5391.

Chapter III: Tubular Filter Fabrication Process

III.1. Kaolin Mixture

III.1.1. Kaolin Mixture Preparation

The preparation of the mixture involved precisely combining equal amounts of DD1 and DD3 kaolin sieved at $200\,\mu m$ to ensure uniformity in composition. The addition of $Amijel$, a specialized binder renowned for its ability to enhance viscosity, played a crucial role in optimizing the paste's workability during shaping processes. Moreover, the inclusion of calcium carbonate ($CaCO_3$) in the blend served the dual purpose of aiding in pore formation and contributing to the overall structural integrity of the material. The exact weight percentage of each component is as follows:

$$\begin{cases} 38\,wt\%\,DD1 \longrightarrow 400.0g \\ 38\,wt\%\,DD3 \longrightarrow 400.0g \\ 20\,wt\%\,CaCO_3 \longrightarrow 210.5g \\ 4\,wt\%\,Amijel \longrightarrow 42.1g \end{cases}$$

This meticulously formulated mixture $1052.6g$ in total ensures not only precise composition but also optimal performance characteristics, laying the foundation for successful fabrication processes.

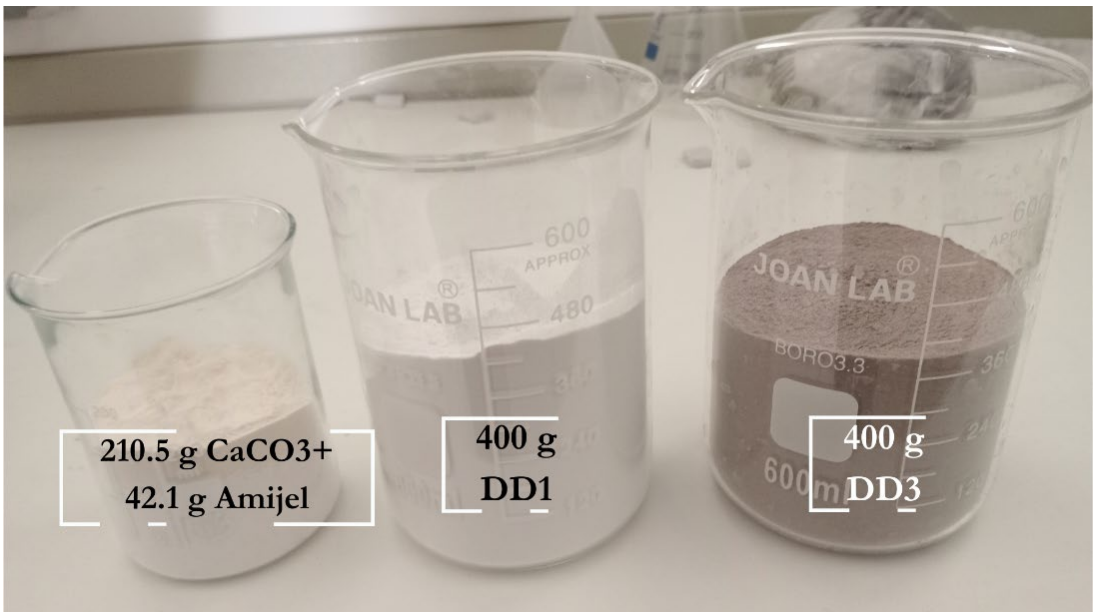

Figure III.1 The Paste Mixture Elements

III.1.2. Paste Creation

An electric blender was employed to thoroughly mix the three powders together. Subsequently, water was gradually added to adjust the rheological properties of the paste, facilitating the shaping process. The incremental addition of water while blending allowed for careful monitoring of the paste's viscosity to ensure it reached the desired consistency without becoming overly viscous. Water was added in increments of 50 milliliters until reaching a total volume of 600 ml.

Figure III.2 KENWOOD 1100W Mixer

After blending for approximately 30 minutes using a KENWOOD 1100W Mixer, and hand mixing as well, and with the incremental addition of water, the paste reached the desired consistency. Subsequently, it was weighed and found to be $1597.8\,g$. The paste was then sealed in plastic bags and left to rest for $\sim 20\ hours$.

Figure III.3 DD1 & DD3 paste

This process was repeated with the same steps to produce another batch of paste, which weighed 801.8 grams. Allowing the paste to rest for 48 hours proved preferable, as it yielded better results.

Table III.1 Chemical Analysis of The Mix

Composition	SiO_2	Al_3O_2	Fe_2O_3	CaO	MgO	SO_3	K_2O
$DD1 + DD2\ (wt\%)$	41.91	37.715	0.09	0.035	0.085	4.645	0.69

III.2. Tubular Configuration Fabrication

III.2.1. Fabrication By Extrusion

A hydraulic shop press, with a 40-ton capacity, was utilized to create the tubular tube components. The method and installation process are detailed in the diagram in Figure III.4. The paste is fed into the press through the top, as shown in the Figure III.5. The piston then applies pressure, and the formed tubular tubes emerge from the other end.

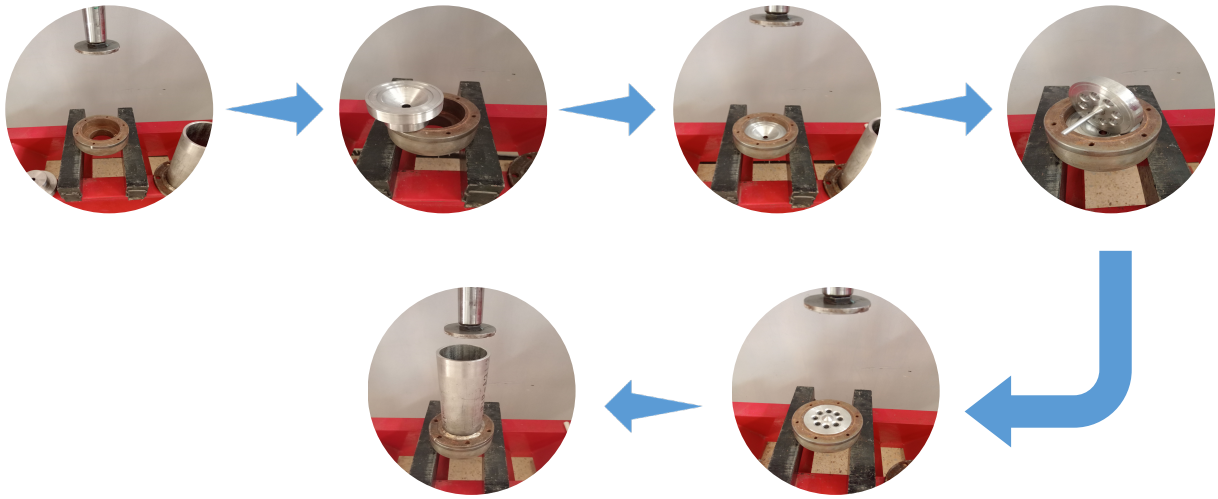

Figure III.4 Extruder Installation Steps

Figure III.5 Shop Press 40 Tons

The resulting tubes are then cut to the appropriate length, less than 40 cm, as shown in Figure III.6. This length limitation is necessary to ensure proper drying during the subsequent process.

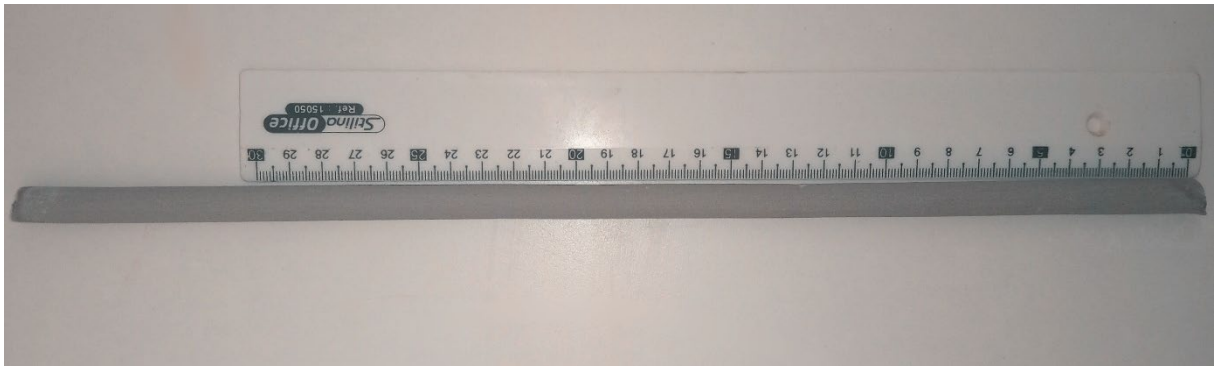

Figure III.6 A Picture of Green Tube

III.2.2. Drying

Previous attempts indicated that an initial air-drying process needs to occur before starting heat treatment due to the high-water content of the tubes. Heat treatment at this stage could cause cracks to form. Additionally, it was found that leaving the tubes to dry on a flat surface resulted in bent tubes and surface cracks. To address this issue, we constructed a roller dryer table using locally available materials from hardware stores, as depicted in Figure III.7.

Figure III.7 Custom-Built Roller Dryer Table

The roller dryer can accommodate four tubes, each 40 centimeters in length, at a time. It is sprayed with starch to prevent the fresh tubes from sticking to the surface and breaking. The dryer is then operated in cycles: it rolls the tubes for 45 minutes, stops for 15 minutes, and then restarts. This cycle continues for around 24 hours.

Figure III.8 Samples After the Initial Drying Process 30 cm Ruler for Reference

This process was repeated for multiple days, yielding 160 centimeters of dried tubes each day, amounting to approximately 800 centimeters in total.

III.2.3. Heat treatment

There were two goals we needed to accomplish with the heating process. The first was to remove the moisture from the green tubes, allowing them to harden and become much tougher, making them capable of withstanding high pressures. The second goal was to remove the calcium carbonate added to the mix, which was intended to enhance the porosity of the tubes.

For the first batch, the heat treatment process was relatively simple. The tubes were heated from room temperature to 1150°C at a rate of 3°C/min and then held in the oven at that temperature for two hours. Afterward, the samples were allowed to cool gradually. However, a problem occurred during the heating process: the tubes bent. Consequently, a revised treatment procedure needed to be designed.

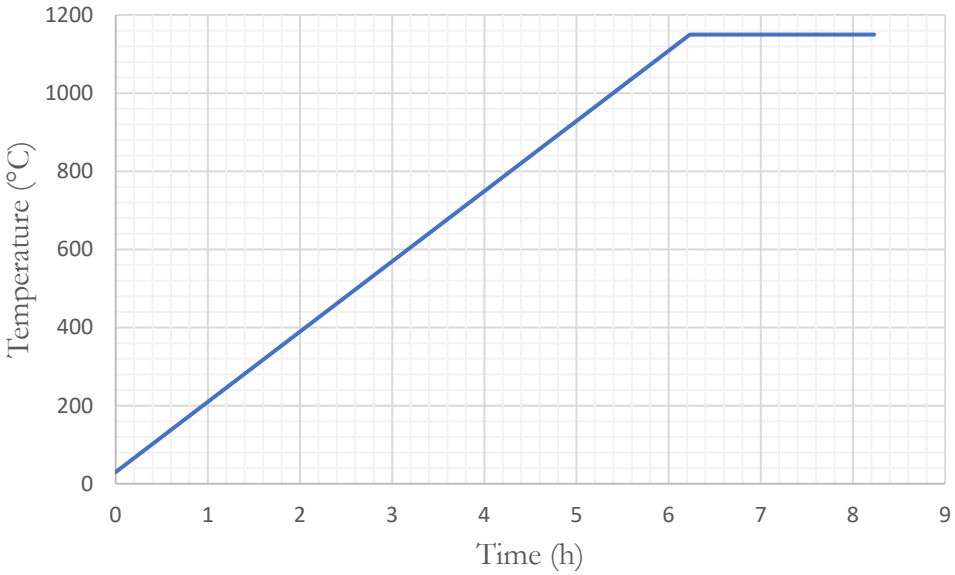

Graph III.1 Heat treatment No.1

The assumption for why the tubes bent during the heating process was that the high heating speed caused compressions within the material and the rapid exit of moisture. Taking this into consideration, a new process was devised.

For this process, a Nabertherm B180 kiln, capable of reaching temperatures up to 1200°C, was used, this kiln features a user-friendly digital controller, allowing precise temperature adjustments and programmable heat-up cycles. Additionally, the kiln's ample chamber size allowed for processing multiple samples simultaneously, enhancing the efficiency of the experimental process.

For this second heat treatment, it was decided to use a heating rate of 2°C/min rather than 3°C/min. The sample was initially heated to 250°C and held at this temperature for half an hour to ensure the removal of moisture from the green body. This step was crucial for preventing structural issues during further heating. After this moisture removal phase, the heating continued at the same rate up to the desired final temperature. Once the final temperature was reached, the sample was held at this temperature for two hours to ensure proper treatment. Three final temperatures were chosen for experimentation: 1150°C, 1175°C, and 1200°C. Follow-up analysis will be conducted to determine which of these temperatures results in the best combination of mechanical properties and permeability.

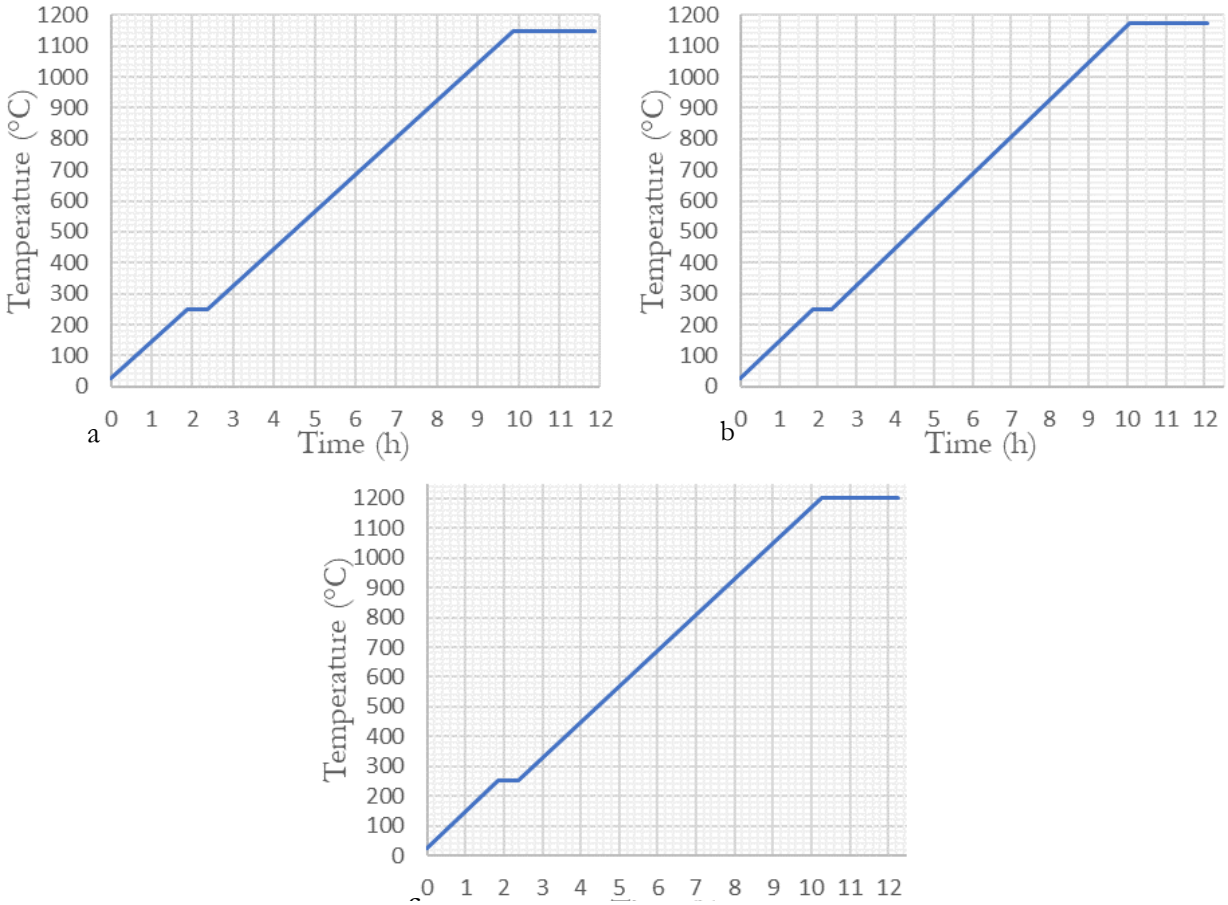

Graph III.2 Heat Treatment Graphs A) Graph Top Temp 1150 °C B) Graph Top Temp 1175 °C C) Graph Top Temp 1200 °C

Chapter IV: Results Discussion and Analysis

IV.1. Chemical analysis

IV.1.1. X-Ray Fluorescence Analysis

This XRF analysis is for the crushed 1150°C tubes. The same device and experimental conditions apply:

Table IV.1 Results of Percentage Oxides from XRF Analysis of the 1150°C Tubes

Composition	SiO_2	Al_3O_2	Fe_2O_3	CaO	MgO	SO_3	K_2O	Na_2O
$Tubes\ at\ 1150°C\ (wt\%)$	62.75	21.22	0.51	0	0.15	1.37	0.46	0

Comparing the compositions before and after heating the tubes at 1150°C reveals significant transformations in the material.

Silica (SiO_2): There is a notable increase in the silica content after heating, indicating a conversion into a silica-rich phase during the thermal treatment.

Alumina (Al_3O_2): The alumina content shows a decrease after heating, suggesting possible reactions or phase transitions involving alumina at high temperatures.

Impurities: Iron oxide and other impurities content remains relatively low and stable, indicating minimal changes during the heating process.

Calcium Carbonate ($CaCO_3$): is significantly reduced after heating, suggesting the decomposition or transformation of calcium-containing compounds at elevated temperatures.

Overall, the changes in composition suggest complex thermal reactions involving the decomposition, transformation, and formation of new phases within the material matrix at elevated temperatures. Further analysis, such as phase identification through techniques like X-ray diffraction (XRD), is necessary to clarify the specific phase transformations occurring during thermal treatment.

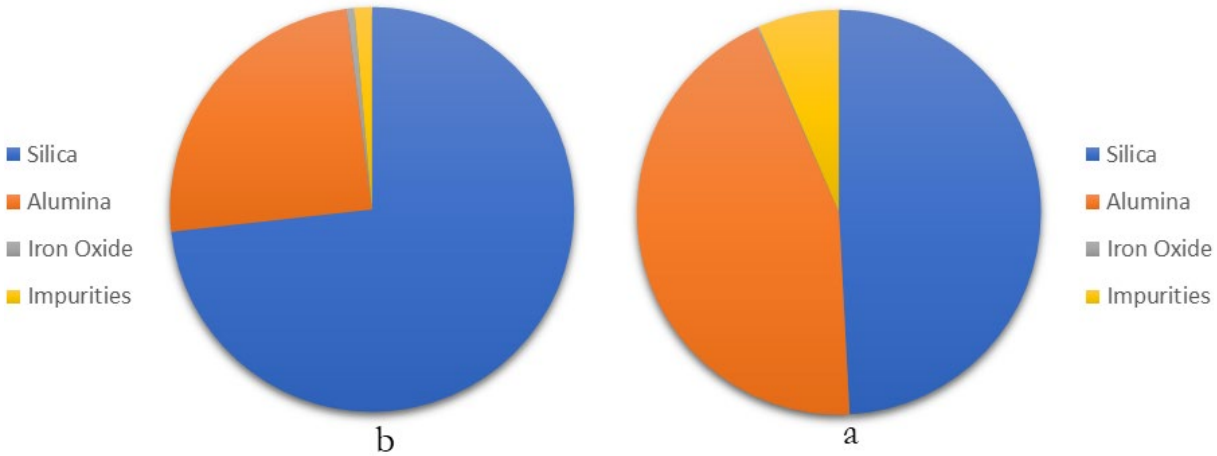

Figure IV.1 Pie Chart Comparing Composition Before (a) and After (b) Heat Treatment

IV.1.2. X-Ray Diffraction Analysis

In this analysis, a different X-ray diffraction analyzer was utilized; this time, we employed the Bruker D8 Series I, as depicted in Figure IV.2. The results of this analysis are presented in Graph IV.1.

Figure IV.2 Bruker D8 Series I XRD- Analyzer

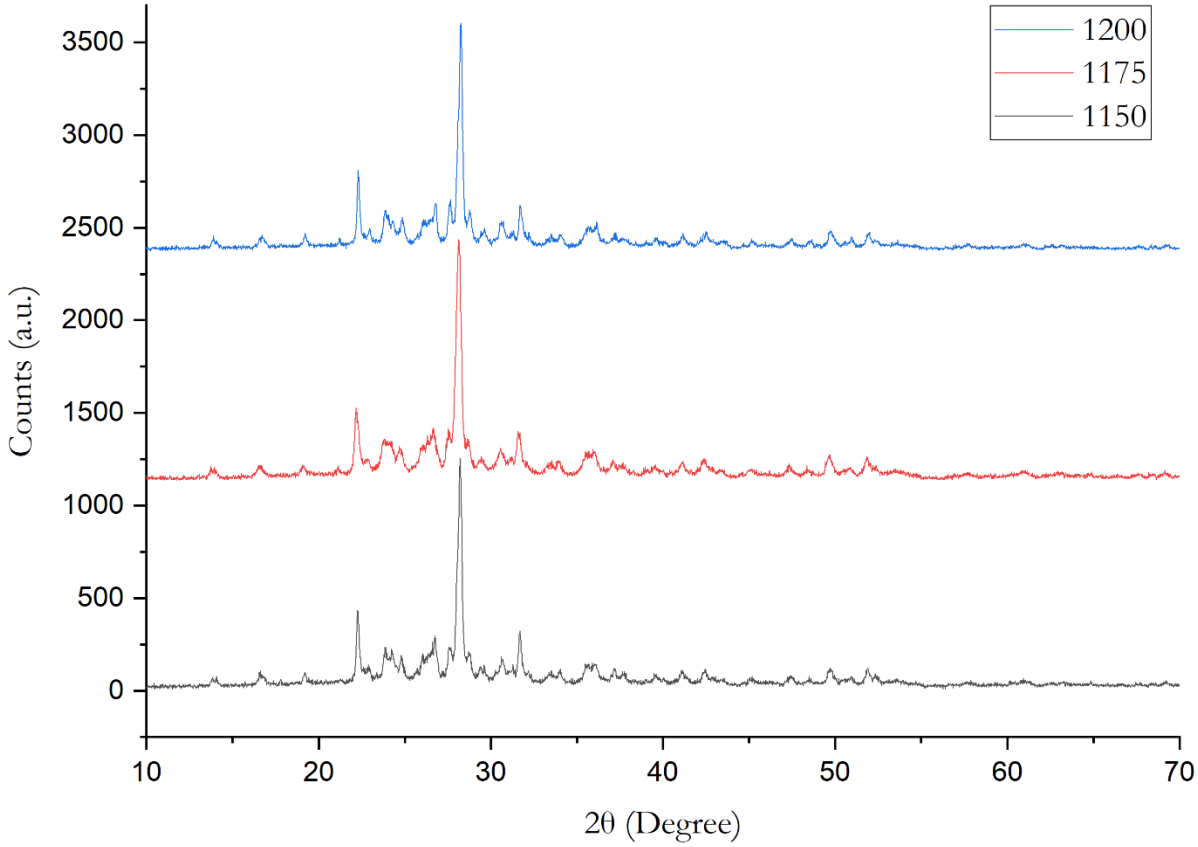

Graph IV.1 XRD Spectra of Three Tube Samples at Different Temperatures

Using HighScore Plus software to analyze Graph IV.1 revealed that that most of the peaks correspond to Mullite. The chemical formula of Mullite is $Al_{4.44}O_{9.78}Si_{1.56}$, and its reference code is 98-009-9327. The remaining peaks likely correspond to Nacrite 6M with the chemical formula $H_4Al_2O_9Si_1$ and the reference code 98-003-1562.

Due to the small temperature differences between each sample, the variation in XRD plots is subtle. However, we observe a slight increase in the Mullite phase with the rise in temperature.

IV.2. Scanning Electron Microscopy (SEM) Imaging

Microscopic examination plays a crucial role in the characterization of materials, offering insights into their morphology, structure, and composition at the micro and nano scales. In this section, we present the results of Scanning Electron Microscopy (SEM) imaging, which provides high-resolution visualization of the sample's surface morphology and microstructure.

Images were acquired using a Thermo Scientific Apreo 2 C Scanning Electron Microscope (SEM), which offers sub-nanometer resolution capabilities for a wide range of materials, including nanoparticles, powders, catalysts, nanodevices, and bulk magnetic samples. (Figure IV.3 displays the instrument located at C.R.A.P.C. – Batna)

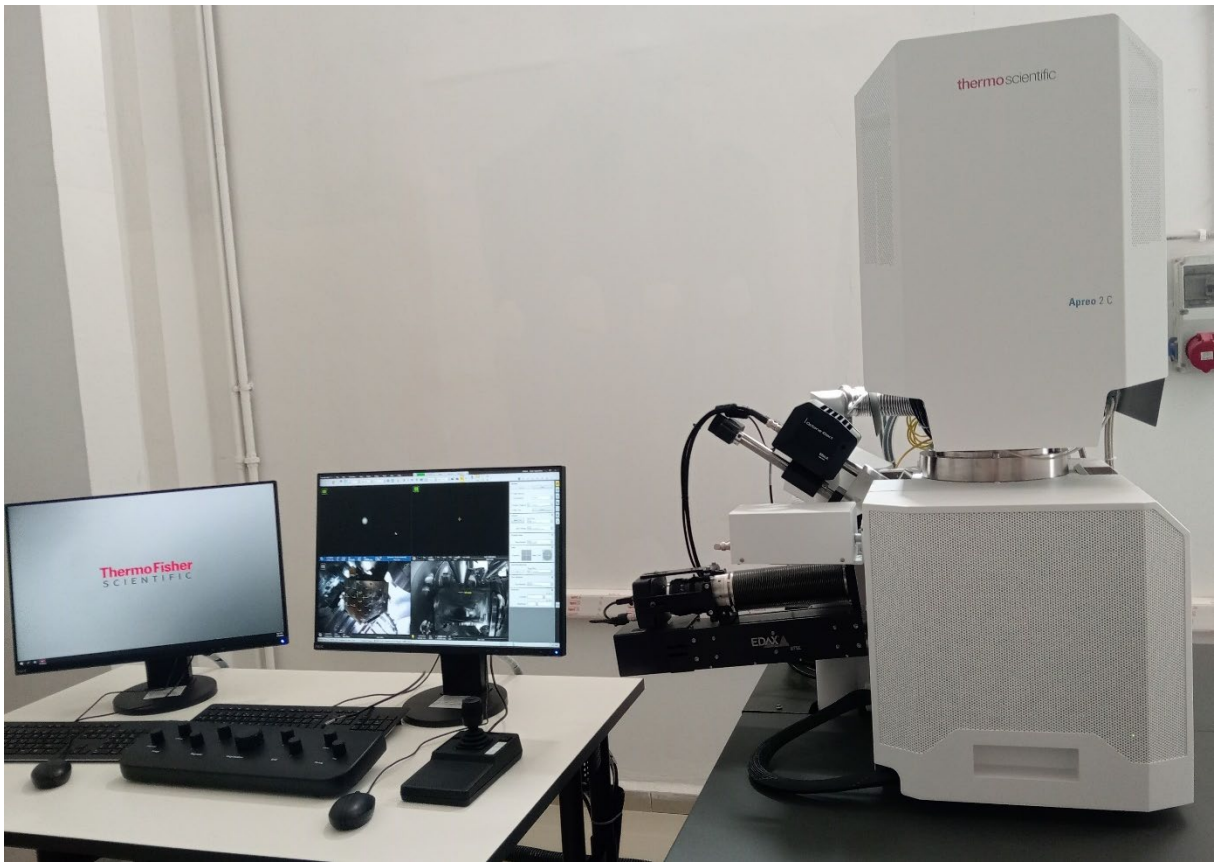

Figure IV.3 Apreo 2 C Scanning Electron Microscope from Thermo Scientific

IV.2.1. Scanning Electron Microscope Images

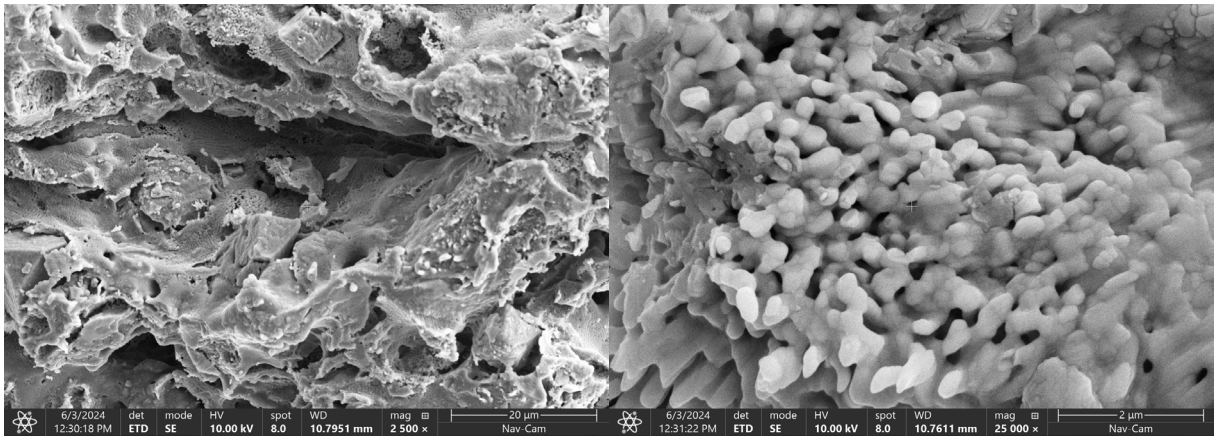

Figure IV.4 Cross-sectional SEM Image of the 1150°C Tubes. Scale bars: 20 µm (left), 2 µm (right)

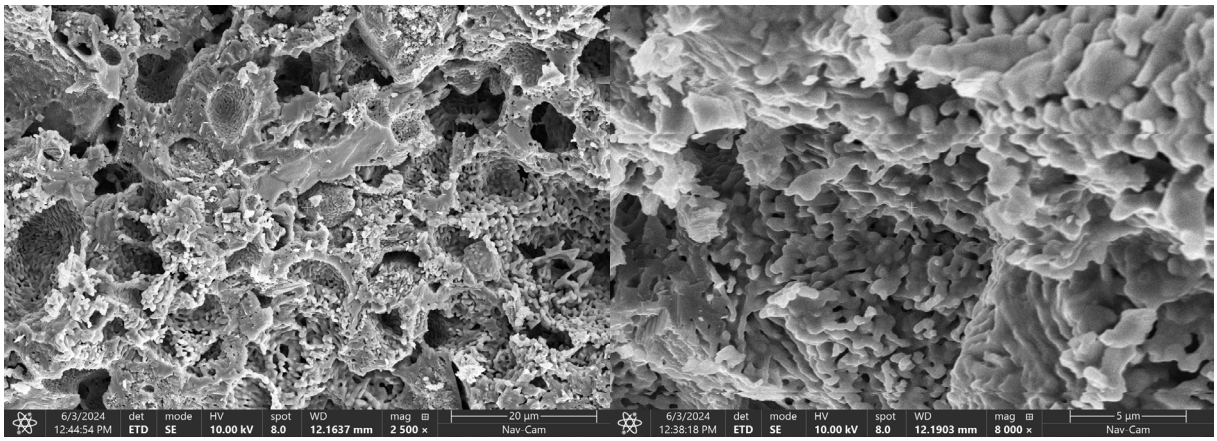

Figure IV.5 Cross-sectional SEM Image of the 1175°C Tubes. Scale bars: 20 µm (left), 5 µm (right)

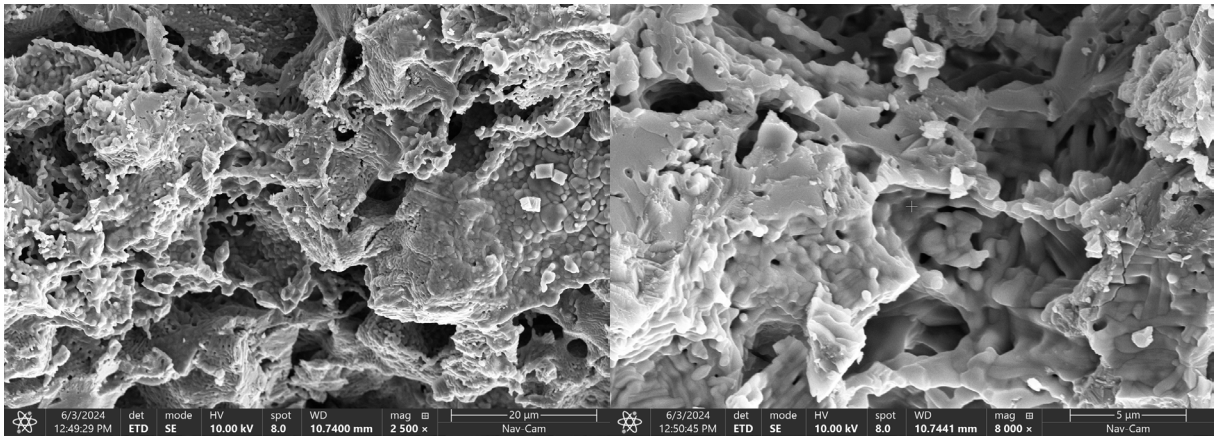

Figure IV.6 Cross-sectional SEM Image of the 1200°C Tubes. Scale bars: 20 µm (left), 5 µm (right)

IV.2.2. Analysis of SEM Images

Through SEM analysis, we aim to uncover key features and details that contribute to a comprehensive understanding of the sample's properties. The following observations from SEM imaging shed light on the intricate characteristics of the material under investigation.

The micro-structure of our porous ceramic, exhibits three-dimensional network structure with strong grain necking [20] (this can be observed in images on the right). Notably, pores and cavities are present in all microstructures, alongside stacked aggregates separated by randomly oriented particles. Pore area showed by the dark/black colors while the clay granules showed by the bright/white colors.[21]

Additionally, the tubular ceramic structure showcases irregularly distributed pores with a relatively complex shape, a characteristic influenced by the material's processing method and its inherent structural arrangement, affirming its highly porous nature. These features, including the random shape of pores and the absence of macro-defects such as cracks, are crucial for ensuring the fabrication of quality supports.[22]

Another hypothesis drawn from the images, later corroborated by the permeability results, is that the filters treated at 1175°C appeared to have the lowest porosity. This observation may be attributed to the increase in sintering temperature, which refines the crystallite size and deforms it to fill the cavities. While this process enhances density, hardness, and tensile strength, it could lead to a decrease in porosity. However, a further increase in temperature to 1200°C might have resulted in pore shifting and merging, as suggested by both the images and permeability results, supporting this hypothesis.

IV.3. Mechanical Properties Analysis

The mechanical strength and pressure endurance of these tubular configurations will determine their viability for higher filtration purposes. Achieving greater mechanical strength while maintaining porosity is essential for advancing to more effective filtration methods, such as nanofiltration or reverse osmosis.

IV.3.1. Flexure/Bend Test

Flexural test data can be particularly useful when a material is to be used as a support structure, in our case a membrane support, to test the flexure strength of the mixture $(48\ wt\%\ DD1 +\ 48\ wt\%\ DD2 + 20\ wt\%\ C_aCO_3 + 4\ wt\%\ Amijel)$, we made ceramic plates from the same mixture, these plates were heated at the same temperatures: $1150°C$, $1175°C\ and\ 1200°C$. The plates had uniform dimensions of 150 mm in length, 13 mm in width, and 6 mm in height.

We used the 5969 Series Universal Testing System from Instron, it's a device capable of a capacity of 50 KN.

Figure IV.7 The 5969 Series Universal Testing System By Instron

- **3-Point Bend Test:** A 3-point flex test balances a specimen between two lower anvils while applying force from a single upper anvil centered at the midpoint. The area of uniform stress is quite small and concentrated under the center loading point. Different testing standards may require the anvils to be fixed, rotated, or rocking, as shown in Figure IV.8. [23]

Figure IV.8 Three-Points Bend Fixture [23]

The results of the analysis can be found in Table IV.2

Table IV.2 Bend Test Analysis Results

Sample's Temperature (°C)	$\sigma_T\ (MPa)$	$\sigma_F\ (MPa)$
1150°C	8.07	21.789
1175°C	9.16	24.732
1200°C	9.32	25.164

- **σ_T (Tensile Stress):**

  Tensile stress is the stress experienced by a material when subjected to a tensile (pulling) force. It is defined as the force applied per unit area. The formula for tensile stress is:

$$\sigma_T = \frac{F_T}{A}$$

where:

σ_T is the tensile stress,

F_T is the tensile force applied,

A is the cross-sectional area of the material.

- **σ_F (Flexural Stress):**

Flexural stress is the stress experienced by a material when subjected to a bending or flexural load. It is defined as the force applied per unit area in the bending situation. The formula for flexural stress is typically:

$$\sigma_F = \frac{M}{S}$$

where:

σ_F is the flexural stress,

M is the bending moment,

S is the section modulus.

IV.3.1.1. Comparison of Flexural and Tensile Stress Between the Three Samples:

- **Sample 1 (1150°C):** has the lowest tensile and flexural stress values among the three samples.
- **Sample 3 (1200°C):** has the highest tensile and flexural stress values.
- **Sample 2 (1175°C):** has intermediate values for both tensile and flexural stress.

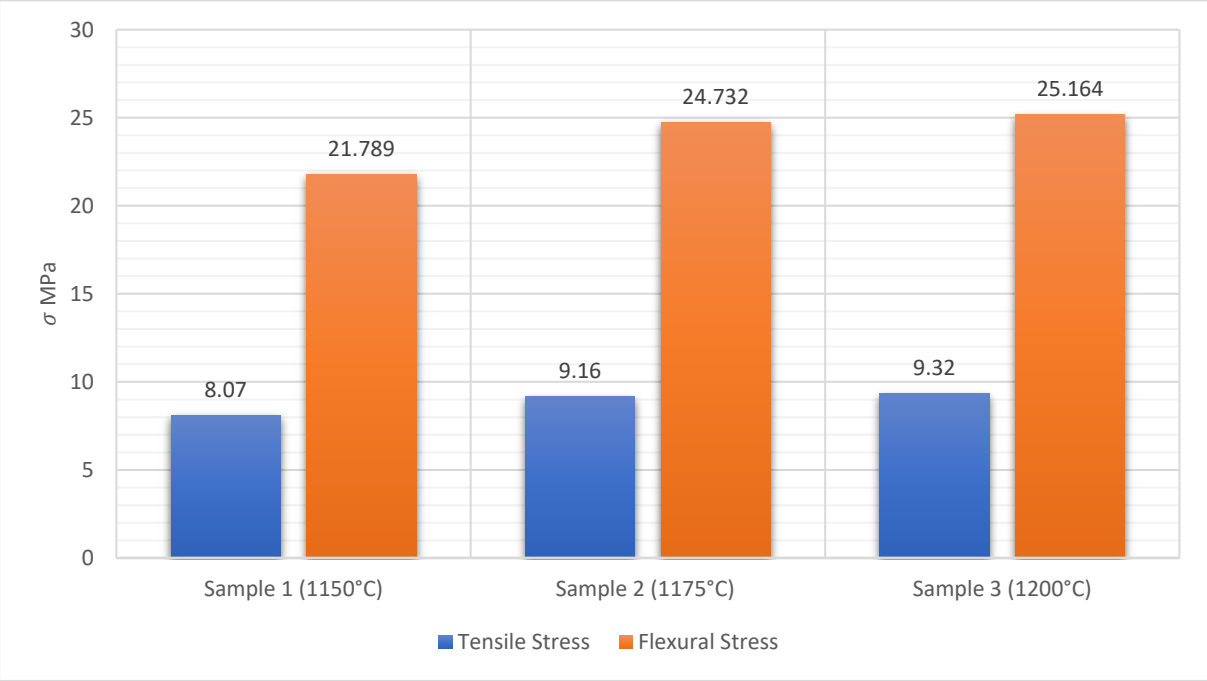

Figure IV.9 Clustered Column Chart Presenting a Comparison Between the Three Samples

These results suggest a positive correlation between processing temperature and mechanical strength in this membrane support material. Samples processed at higher temperatures (1200°C) exhibited greater tensile and flexural stress compared to those processed at lower temperatures (1150°C). This could translate to stronger support for the membranes themselves. Further investigations, such as porosity analysis or permeability studies, are necessary for a comprehensive understanding of how these properties affect the overall performance of the membrane system.

IV.4. Permeability Test

Before conducting the permeability test, we ensured that the filtration tubes were submerged in distilled water for a period of 24 hours or more. Special housing modules were then fabricated from copper to conduct this test, as shown in Figure IV.10.

Figure IV.10 Housing Modules for The Filtration Tubes

The testing apparatus was assembled using components available at hardware stores, as depicted in Figure IV.11. All subsequent experiments were conducted under standard conditions, with ice bottles placed inside the container to keep the water cold and prevent overheating of the pump due to high pressure.

The test involved measuring the duration it took for the tubular configuration to fill a 20 or a 10-milliliter tube with distilled water at 4-minute intervals. This experiment was conducted for each tube (1150°C, 1175°C, and 1200°C) under different pressures of 0.6, 0.8, and 1 bar, Other experimental conditions are summarized above each table of the results.

Figure IV.11 Custom Made Filtration Permeability Tester

IV.4.1. Permeability Results for the 1150°C Tubes:

For this procedure, the tube length was 130 millimeters, and the radius was 4.5 millimeters, resulting in a filtration area of $3.676 \times 10^{-3}\ m^2$. The volume of the tube was 20 milliliters. We can use this information to calculate the permeability using the following equation:

$$\phi = \frac{V}{S \times T} \left({}^{l}/_{m^2.h}\right) \dots\dots\dots\dots\dots (1)$$

Where:

ϕ: Permeability (liters per square meter per hour)

V: Volume permeable through the filter in liters

S: Area that is permeable through in square meters

T: Duration to fill the volume in hours

We summarize the results in the following three tables:

Table IV.3 Permeability Trends Across Time Intervals for the 1150°C Tubes At 0.6 Bar

Time Intervals (min)	0	4	8	12	16	20	24	28	32	36
Duration (s)	190	201	207	200	196	197	199	198	197	196
Permeability ${}^{l}/_{m^2.h}$	103	97	95	98	100	99	98	99	99	100

Table IV.4 Permeability Trends Across Time Intervals for the 1150°C Tubes At 0.8 Bar

Time Intervals (min)	0	4	8	12	16	20	24	28	32	36
Duration	71	82	93	85	92	92	95	96	94	95
Permeability ${}^{l}/_{m^2.h}$	276	239	211	230	213	213	206	204	208	206

Table IV.5 Permeability Trends Across Time Intervals for the 1150°C Tubes At 1.0 Bar

Time Intervals (min)	0	4	8	12	16	20	24	28	32	36
Duration (s)	63	52	57	60	63	66	65	64	65	63
Permeability ${}^{l}/_{m^2.h}$	377	356	344	326	311	297	301	306	301	311

We summarize the permeability trends from these tables in Graph IV.2, which illustrates the change in permeability with time intervals. By plotting these data points, we can observe how permeability varies as different pressures are applied.

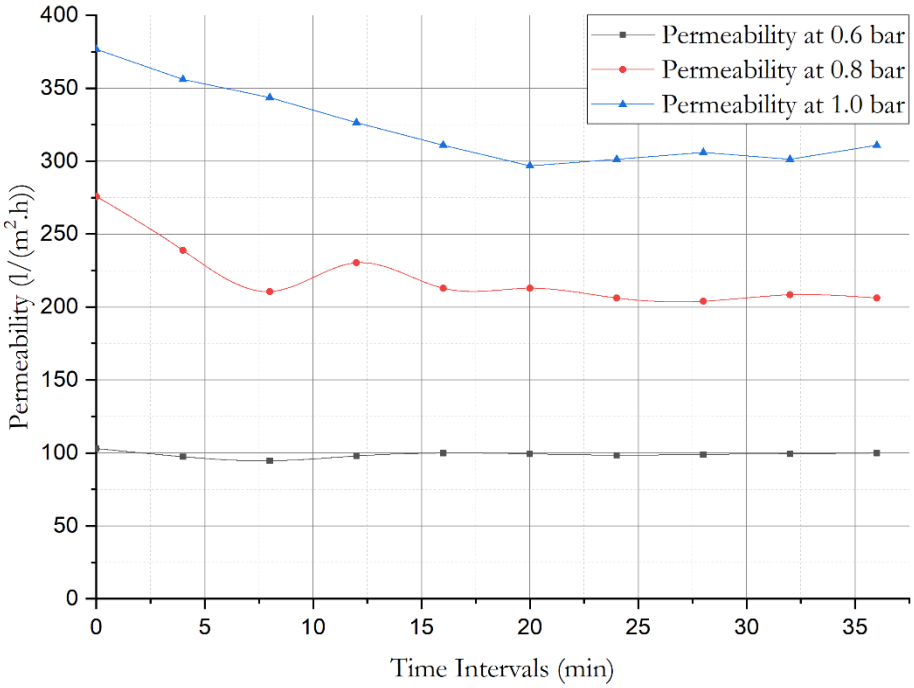

Graph IV.2 Variation of Permeability Over Time at Different Pressures for the 1150°C Tubes

From these tables, we can calculate the average permeability of the last seven points at each pressure as follows:

$$\begin{cases} 0.6\ bar \rightarrow 99\ {}^{l}/_{m^2.h} \\ 0.8\ bar \rightarrow 212\ {}^{l}/_{m^2.h} \\ 1.0\ bar \rightarrow 308\ {}^{l}/_{m^2.h} \end{cases}$$

These values enable us to plot Graph IV.3, which represents the relationship between permeability and pressure. The coefficient of permeability can be determined from the slope of the graph.

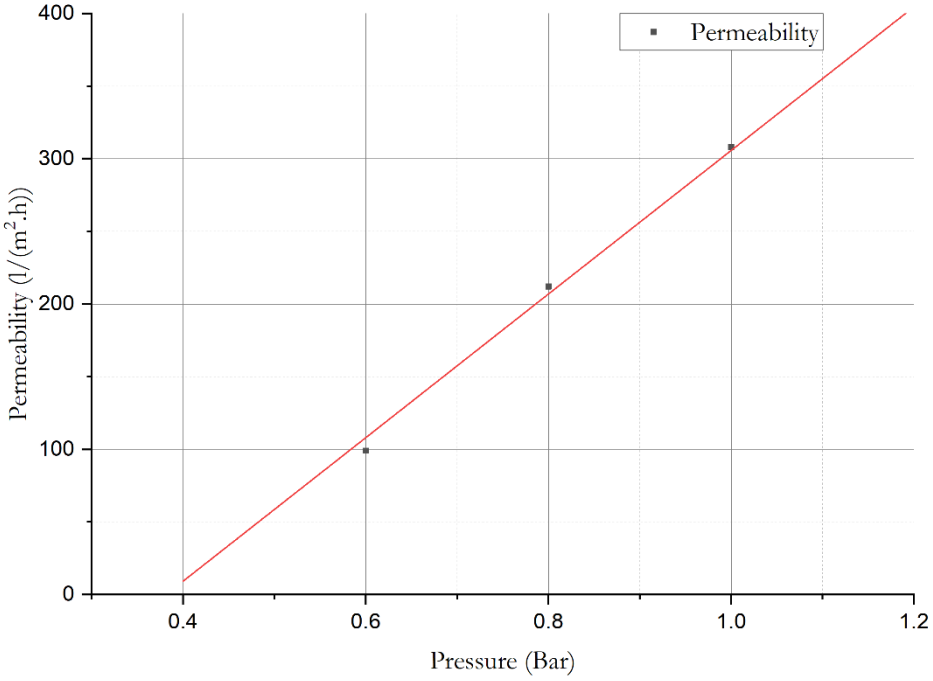

Graph IV.3 Average Permeability Change with Respect to Pressure for the 1150°C Tubes

Using two points from the graph line, we can calculate the equation of the straight line, which is:

$$\phi = 494.17 \times P - 188.48$$

Where:

ϕ: Permeability (liters per square meter per hour)

P: Pressure (bar)

From this, we deduce that the permeability coefficient for the 1150°C tubes is:

$$\Phi = 494.17 \ {}^{l}/_{m^2.h.bar}$$

We can also determine that the pressure at which the permeability is zero is P = 0.3811 bar.

IV.4.2. Permeability Results for the 1175°C Tubes:

For this procedure, the tube length was 80 millimeters, and the radius was 4.5 millimeters, resulting in a filtration area of $2.262 \times 10^{-3}\ m^2$. The volume of the tube was 20 milliliters for 0.8 bar and 10 milliliters for 0.6 and 1.0 bar. We can use this information to calculate the permeability using equation (1), The results can be found in the following tables:

Table IV.6 Permeability Trends Across Time Intervals for the 1175°C Tubes At 0.6 Bar

Time Intervals (min)	0	4	8	12	16	20	24	28	32	36
Duration (s)	79	102	111	120	125	129	126	129	127	126
Permeability ${}^{l}/_{m^2.h}$	201	156	143	133	127	123	126	123	125	126

Table IV.7 Permeability Trends Across Time Intervals for the 1175°C Tubes At 0.8 Bar

Time Intervals (min)	0	4	8	12	16	20	24	28	32	36
Duration (s)	108	115	122	135	141	157	160	162	158	159
Permeability ${}^{l}/_{m^2.h}$	295	277	261	236	226	203	199	196	201	200

Table IV.8 Permeability Trends Across Time Intervals for the 1175°C Tubes At 1.0 Bar

Time Intervals (min)	0	4	8	12	16	20	24	28	32	36
Duration (s)	54	57	56	54	55	55	56	55	56	54
Permeability ${}^{l}/_{m^2.h}$	295	279	284	295	289	289	284	289	284	295

We summarize the permeability trends from these tables in Graph IV.4, which illustrates the change in permeability with time intervals. By plotting these data points, we can observe how permeability varies as different pressures are applied.

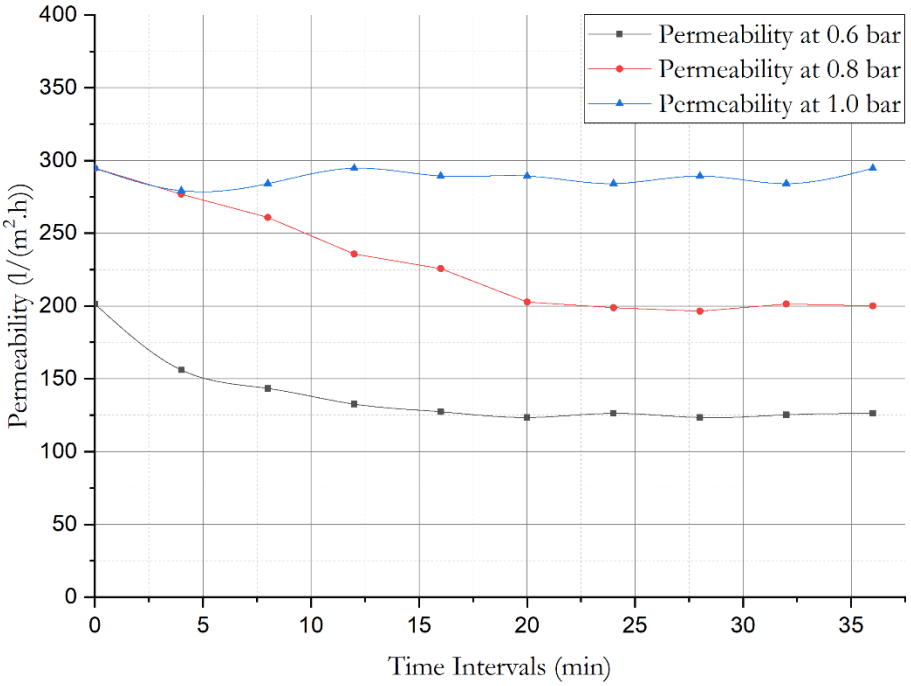

Graph IV.4 Variation of Permeability Over Time at Different Pressures for the 1175°C Tubes

From these tables, we can calculate the average permeability of the last seven points at each pressure as follows:

$$\begin{cases} 0.6\ bar \rightarrow 126\ {}^{l}/_{m^2.h} \\ 0.8\ bar \rightarrow 209\ {}^{l}/_{m^2.h} \\ 1.0\ bar \rightarrow 289\ {}^{l}/_{m^2.h} \end{cases}$$

These values enable us to plot Graph IV.5, which represents the relationship between permeability and pressure. The coefficient of permeability can be determined from the slope of the graph.

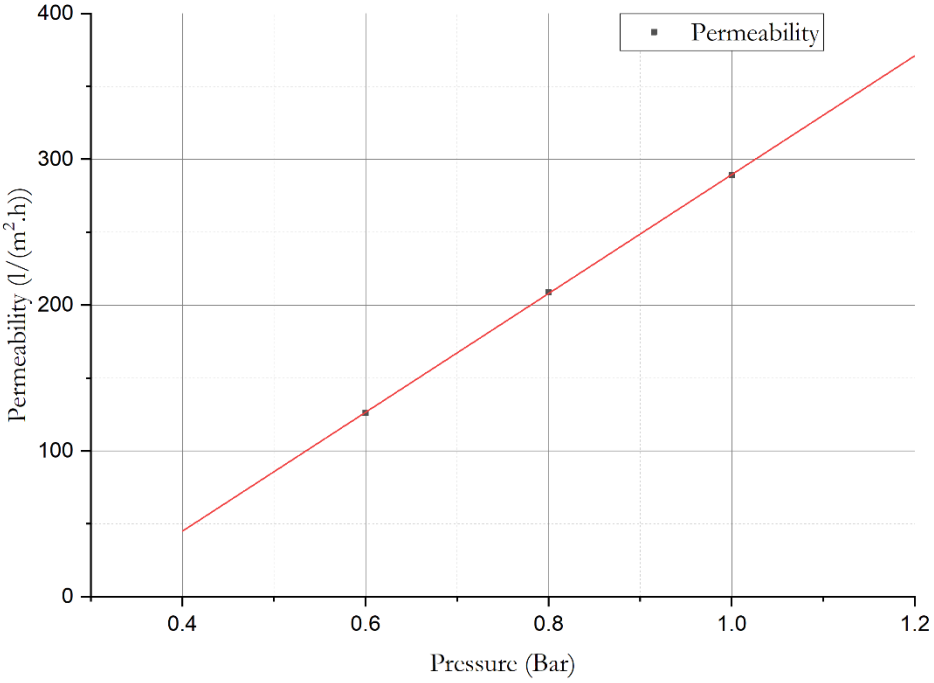

Graph IV.5 Average Permeability Change with Respect to Pressure for the 1175°C Tubes

Using two points from the graph line, we can calculate the equation of the straight line, which is:

$$\phi = 407.5 \times P - 118$$

Where:

ϕ: Permeability (liters per square meter per hour)

P: Pressure (bar)

From this, we deduce that the permeability coefficient for the 1150°C tubes is:

$$\Phi = 407.5 \ {}^{l}/_{m^2.h.bar}$$

We can also determine that the pressure at which the permeability is zero is P = 0.2896 bar.

IV.4.3. Permeability Results for the 1200°C Tubes:

For this procedure, the tube length was 79 millimeters, and the radius was 4.5 millimeters, resulting in a filtration area of $2.234 \times 10^{-3} \ m^2$. The volume of the tube was 20 milliliters for 0.6 bar and 10 milliliters for 0.8 and 1.0 bar. We can use this information to calculate the permeability using equation (1).

Table IV.9 Permeability Trends Across Time Intervals for the 1200°C Tubes At 0.6 Bar

Time Intervals (min)	0	4	8	12	16	20	24	28	32	36
Duration (s)	290	293	295	295	293	294	295	294	293	294
Permeability ${}^{l}/_{m^2.h}$	109	110	110	109	110	110	109	110	110	110

Table IV.10 Permeability Trends Across Time Intervals for the 1200°C Tubes At 0.8 Bar

Time Intervals (min)	0	4	8	12	16	20	24	28	32	36
Duration (s)	83	85	87	90	89	91	90	89	89	90
Permeability ${}^{l}/_{m^2.h}$	194	190	185	179	181	177	179	181	181	179

Table IV.11 Permeability Trends Across Time Intervals for the 1200°C Tubes At 1.0 Bar

Time Intervals (min)	0	4	8	12	16	20	24	28	32	36
Duration (s)	48	49	54	53	52	54	55	53	54	53
Permeability ${}^{l}/_{m^2.h}$	336	329	298	304	310	298	293	304	298	304

We summarize the permeability trends from these tables in Graph IV.6, which illustrates the change in permeability with time intervals. By plotting these data points, we can observe how permeability varies as different pressures are applied.

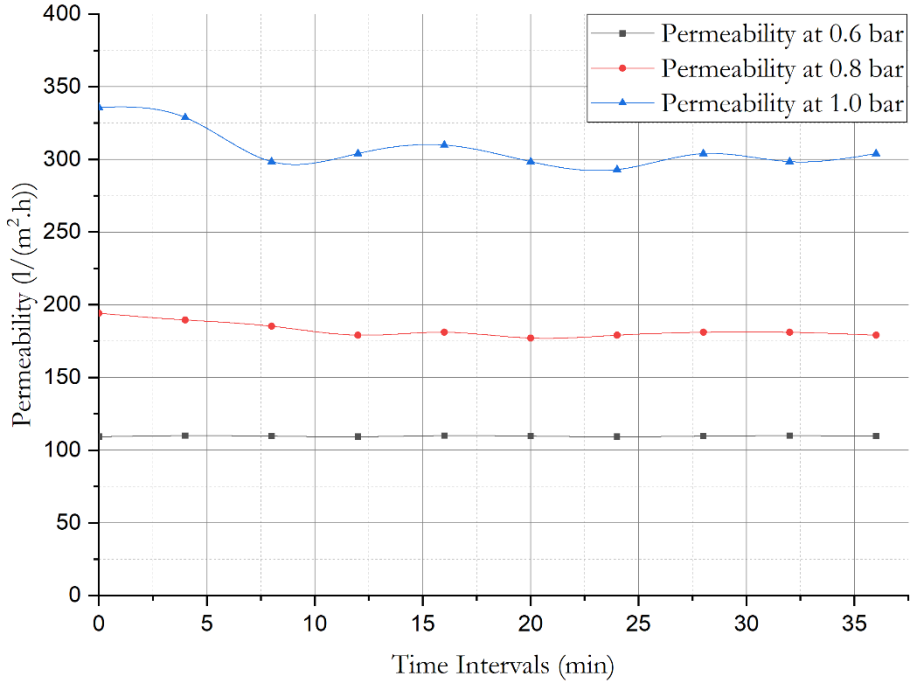

Graph IV.6 Variation of Permeability Over Time at Different Pressures for the 1200°C Tubes

From these tables, we can calculate the average permeability of the last seven points at each pressure as follows:

$$\begin{cases} 0.6\ bar \rightarrow 110\ {}^{l}/_{m^2.h} \\ 0.8\ bar \rightarrow 180\ {}^{l}/_{m^2.h} \\ 1.0\ bar \rightarrow 302\ {}^{l}/_{m^2.h} \end{cases}$$

These values enable us to plot Graph IV.7, which represents the relationship between permeability and pressure. The coefficient of permeability can be determined from the slope of the graph.

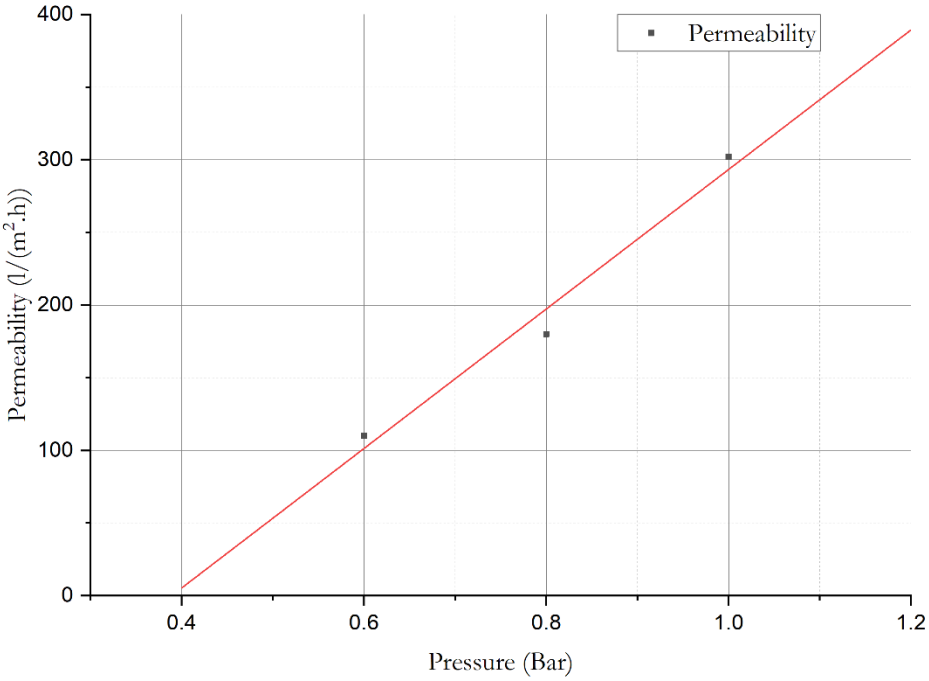

Graph IV.7 Average Permeability Change with Respect to Pressure for the 1175°C Tubes

Using two points from the graph line, we can calculate the equation of the straight line, which is:

$$\phi = 480 \times P - 186.67$$

Where:

ϕ: Permeability (liters per square meter per hour)

P: Pressure (bar)

From this, we deduce that the permeability coefficient for the 1150°C tubes is:

$$\Phi = 480 \ {}^{l}/_{m^2.h.bar}$$

We can also determine that the pressure at which the permeability is zero is P = 0.388 bar.

IV.4.4. Comparing the Results

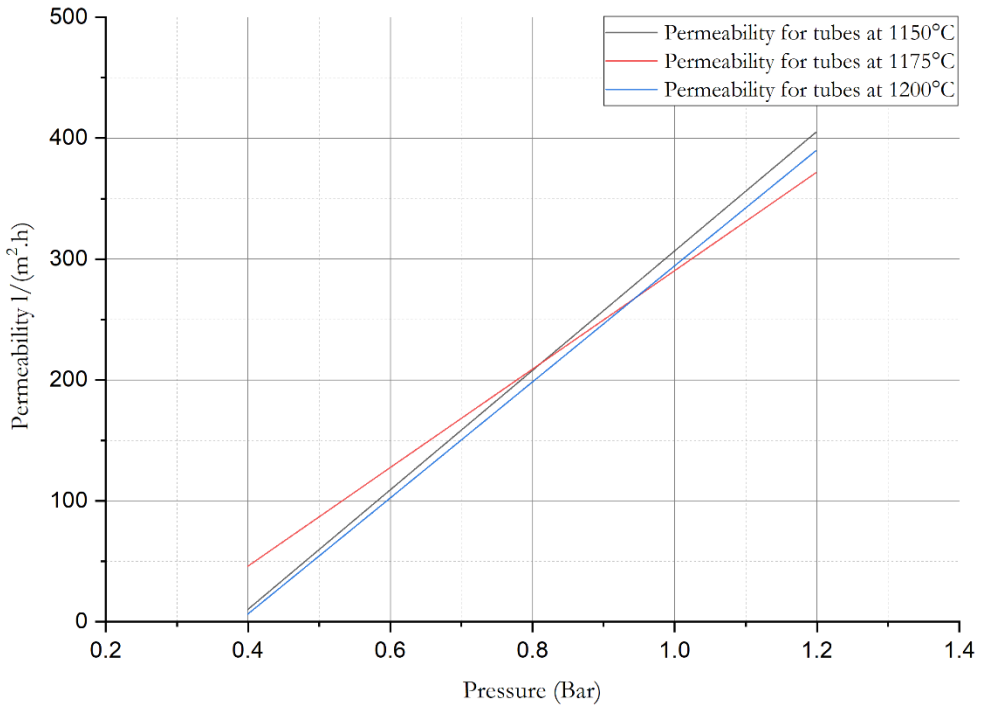

Graph IV.8 Average Permeability Change with Respect to Pressure Comparison Graph

Upon analysis of the three values of the permeability coefficient and referring to Graph IV.8, it becomes evident that the tubes treated at 1150°C exhibit the highest permeability, followed by those treated at 1200°C, and lastly, those treated at 1175°C. This observation could be clarified by the SEM results, suggesting that the rise in temperature from 1150°C to 1175°C may have resulted in pore closure. Subsequently, the further increase in temperature to 1200°C likely induced pore shifting and merging, consequently leading to the spike in permeability. This suggests that the tubes treated at 1175°C are likely to possess the highest filtration capabilities but the lowest permeability.

$$\begin{cases} 407.5 \ {}^{l}/_{m^2.h.bar} < 480 \ {}^{l}/_{m^2.h.bar} < 494.1 \ {}^{l}/_{m^2.h.bar} \\ \Phi_{1175°C} < \Phi_{1200°C} < \Phi_{1150°C} \end{cases}$$

IV.4.4.1. Comparing Permeability Results with Previous Studies

Upon reviewing the relevant literature, it is noted that one of the most common higher-end permeability coefficient results reported is $\Phi = 1440\ {}^{l}/_{m^2.h.bar}$ [5], a value considerably larger than our findings. However, while our permeability may be lower, we compensate with enhanced mechanical strength and a smaller pore size, both of which contribute to serving as both a better support and as an independent filter.

Another notable detail is the initial spike in permeability values upon the application of pressure, followed by a subsequent decline and stabilization. This phenomenon could be attributed to the filters being initially submerged in distilled water.

IV.5. Filtration Test

To evaluate the filtration efficiency of our fabricated tubes, a water sample known to contain copper corrosion products was utilized. The sample, exhibiting a characteristic yellowish-red discoloration (Figure IV.12), was obtained from a pump where water had stagnated for an extended period. The filtration apparatus depicted in Figure IV.11 was employed, applying a controlled pressure to the sample solution. The results of this filtration experiment are presented in Figure IV.12.

Figure IV.12 (a) Corrosion tainted sample (b) Results after filtration

Comparison of Water Samples. (a) The original water sample displays a characteristic yellowish discoloration, indicative of the presence of suspended particulate matter. (b) Following filtration through our ceramic tubes (all three tubes gave the same results), the water sample regains its clarity, demonstrating the effectiveness of the filtration process in removing the discoloring agents.

Conclusion

In conclusion, this study aimed to comprehensively characterize local ceramic materials, optimize the ceramic preparation process, and evaluate the durability and microfiltration capabilities of ceramic tubes. Throughout the research process, our primary objectives were to analyze the structural and chemical composition of the ceramic materials and thoroughly document the methodologies employed.

The selection of ceramics was predicated on their notable attributes, including robust mechanical resilience, chemical inertness, prolonged operational longevity, and thermal stability. Additionally, their widespread availability at an affordable cost renders them a valuable resource ripe for exploitation. Furthermore, their diverse array of industrial applications underscores their significance as a subject meriting thorough investigation.

This study commenced with an examination of the fundamental properties and distinctive characteristics of ceramics, providing essential context for our research. Subsequently, our focus shifted towards membranes, where we explored their various types and underscored their pivotal role in achieving advanced filtration levels such as ultrafiltration.

Turning our attention to membrane supports, we emphasized their critical significance in membrane technology. We explored the diverse configurations in which these supports are engineered. including tubular, hollow-fiber, and spiral wound designs. Additionally, we delved into the myriad manufacturing methods employed in producing membrane supports, shedding light on the intricacies of their fabrication processes, such as extrusion, pressing slip casting.

Following the acquisition of locally sourced kaolin from the Jebel Debagh mine in Roknia, Guelma, our study embarked on a comprehensive examination of this material. The preparation process commenced with grinding, calcination, and sieving of the samples, laying the groundwork for subsequent analyses. A meticulous chemical analysis was undertaken to unravel the properties of this invaluable resource.

The Fourier-transform infrared spectroscopy (FTIR) analysis unveiled crucial bonds, including hydroxyl *(O-H)*, silicon-oxygen *(Si-O-Si)*, aluminum hydroxide *(Al-OH)*, and silicate *(Si-O & Si-O-Al)*. A comparative assessment post-calcination revealed a reduction in *hydroxyl O-H* values attributed to water evaporation and shifts in crystalline structure explaining other reductions.

Subsequently, TGA/DSC Analysis explained the material's transformations under varying temperatures. This analysis provided insights into the thermal behavior and stability of the kaolin samples.

Moreover, X-ray fluorescence (XRF) analysis demonstrated the high purity and abundance of alumina and quartz in the material. These findings were corroborated by X-ray diffraction (XRD) results, which identified the predominant phases, predominantly consisting of Kaolinite 1A, reaffirming the composition of the kaolin samples.

In our exploration of the manufacturing method for the tubular configuration, we detailed the composition of the kaolin mixture, comprising $38\ wt\%\ DD1\ and\ DD3$, $20\ wt\%\ CaCO_3\ and\ 4\ wt\%\ Amijel$. The paste creation process and the fabrication steps by extrusion were meticulously outlined. To facilitate the drying process, a custom roller dryer table was constructed using locally available materials, followed by a specialized heat treatment process.

In the fourth and final chapter, we delved into our findings, commencing with the chemical analysis of our tubular filters. X-ray fluorescence analysis revealed a notable transformation, with silica content increasing from $42\ wt\%$ to $62\ wt\%$ and the decrease in alumina content from $37\ wt\%$ to $21\ wt\%$ This transition was accompanied by a phase shift predominantly to the Mullite phase, as confirmed by X-ray diffraction. SEM images unveiled a three-dimensional network structure with robust grain necking, illuminating the high durability of the filters. Moreover, the presence of pores and cavities in all microstructures underscored the inherent porosity of our tubes.

Subsequent mechanical properties analysis demonstrated that tubes treated at higher temperatures, such as 1200°C, exhibited superior flexural and tensile stress values compared to those treated at 1175°C and 1150°C. This correlation suggests that higher treatment temperatures correspond to increased mechanical strength. However, permeability results indicated a negative impact on permeability at higher temperatures, despite the enhanced mechanical strength.

Finally, filtration tests demonstrated the effectiveness of these filters in removing suspended particles at the microfiltration level, confirming their practical applicability in filtration processes. However, further investigations are warranted to assess their potential for higher filtration levels. Additionally, studies are needed to determine the porosity and porosity distribution of the tubes, as current testing capabilities are limited in this regard.

References

[1] F. Bouzerara, A. Harabi, S. Achour, and A. Larbot, “Porous ceramic supports for membranes prepared from kaolin and doloma mixtures,” *J Eur Ceram Soc*, vol. 26, no. 9, pp. 1663–1671, Jan. 2006, doi: 10.1016/j.jeurceramsoc.2005.03.244.

[2] A. G. Fane, C. Y. Tang, and R. Wang, “Membrane Technology for Water: Microfiltration, Ultrafiltration, Nanofiltration, and Reverse Osmosis,” in *Treatise on Water Science*, Elsevier, 2011, pp. 301–335. doi: 10.1016/B978-0-444-53199-5.00091-9.

[3] Richard W. Baker, *Membrane Technology and Applications*, 3rd ed. John Wiley and Sons Ltd, 2012.

[4] S.-H. Lee, K.-C. Chung, M.-C. Shin, J.-I. Dong, H.-S. Lee, and K. H. Auh, “Preparation of ceramic membrane and application to the crossflow microfiltration of soluble waste oil,” *Mater Lett*, vol. 52, no. 4–5, pp. 266–271, Feb. 2002, doi: 10.1016/S0167-577X(01)00405-0.

[5] B. Boudaira, A. Harabia, F. Bouzerara, and S. Condom, “Preparation and characterization of microfiltration membranes and their supports using kaolin (DD2) and CaCO 3,” *Desalination Water Treat*, vol. 9, no. 1–3, pp. 142–148, Sep. 2009, doi: 10.5004/dwt.2009.764.

[6] W. M. Barsoum, *Fundamentals of Ceramics*, 1st ed. London: Institute of Physics Publishing, 2003.

[7] W. A. Deer, R. A. Howie, and J. Zussman, *An Introduction to the Rock-Forming Minerals*, 3rd ed. Mineralogical Society of Great Britain and Ireland, 2013. doi: 10.1180/DHZ.

[8] “Alumina Tubes – CeramTec,” https://precision-ceramics.com/eu/advanced-ceramic-tubes/

[9] C. B. Carter and M. G. Norton, *Ceramic Materials: Science and Engineering*, 1st ed., vol. 716. New York: Springer, 2007.

[10] C. Charcosset, *Membrane Processes in Biotechnology and Pharmaceutics*, 1st ed. Elsevier, 2012. doi: 10.1016/C2011-0-04261-8.

[11] Nicholas Hankins and Singh Rajindar, *Emerging Membrane Technology for Sustainable Water Treatment*. Elsevier Science, 2016.

[12] E. K. Lee and W. J. Koros, "Membranes, Synthetic, Applications," in *Encyclopedia of Physical Science and Technology*, 3rd ed., R. A. Meyers, Ed., Elsevier, 2003, pp. 279–344. doi: 10.1016/B0-12-227410-5/00419-1.

[13] بوجمعة، غويل, "تحضير ودراسة مرشحات خزفية مصنعة من مواد أولية محلية, مذكرة دكتوراه," جامعة جيجل, جيجل, 2015.

[14] L. W. McKeen, *Permeability Properties of Plastics and Elastomers*, 3rd ed. William Andrew, 2012. doi: 10.1016/C2010-0-66502-3.

[15] D. Ewis, N. A. Ismail, M. Hafiz, A. Benamor, and A. H. Hawari, "Nanoparticles functionalized ceramic membranes: fabrication, surface modification, and performance," *Environmental Science and Pollution Research*, vol. 28, no. 10, pp. 12256–12281, Mar. 2021, doi: 10.1007/s11356-020-11847-0.

[16] Y. Zhang, Y. Tan, R. Sun, and W. Zhang, "Preparation of Ceramic Membranes and Their Application in Wastewater and Water Treatment," *Water (Basel)*, vol. 15, no. 19, p. 3344, Sep. 2023, doi: 10.3390/w15193344.

[17] W.-B. Kim, S.-C. Kwon, S.-H. Cho, and J.-H. Lee, "Effect of Pressing Process on the High-Temperature Stability of Yttria-Stabilized Zirconia Ceramic Material in Molten Salt of CaCl2-CaF2-CaO," *Korean Journal of Materials Research*, vol. 30, no. 4, pp. 176–183, Apr. 2020, doi: 10.3740/MRSK.2020.30.4.176.

[18] J. A. Queiroga, E. H. M. Nunes, D. F. Souza, D. C. L. Vasconcelos, V. S. T. Ciminelli, and W. L. Vasconcelos, "Microstructural investigation and performance evaluation of slip-cast alumina supports," *Ceram Int*, vol. 43, no. 4, pp. 3824–3830, Mar. 2017, doi: 10.1016/j.ceramint.2016.12.037.

[19] M. Laraba and A. Roula, " Transform Infrared Spectroscopy (FTIR) Structural characterization of kaolin from Djebel Debbagh Mine using Fourier Transform Infrared Spectroscopy (FTIR) aolin from Djebel Debbagh Mine using Fourier Transform Infrared Spectroscopy (FTIR)," *Research Journal of Material Sciences*, vol. 7, no. 3, pp. 1–6, Sep. 2019.

[20] T. Ohji and M. Fukushima, “Macro-porous ceramics: processing and properties,” *International Materials Reviews*, vol. 57, no. 2, pp. 115–131, Mar. 2012, doi: 10.1179/1743280411Y.0000000006.

[21] A. Nurmiyanto and A. Prasetya, “Investigation of Locally Made Ceramic Filter for Household Water Treatment,” *Jurnal Sains &Teknologi Lingkungan*, vol. 4, no. 2, pp. 88–100, Sep. 2012, doi: 10.20885/jstl.vol4.iss2.art3.

[22] D. da S. Biron, J. Bortoluz, M. Zeni, C. P. Bergmann, and V. dos Santos, “Characterization of Mullite Ceramic Membranes and their Application in the Removal Escherichia Coli,” *Materials Research*, vol. 19, no. 3, pp. 513–519, Apr. 2016, doi: 10.1590/1980-5373-MR-2015-0301.

[23] “Test Types: Flexural-Testing,” https://www.instron.com/en/resources/test-types/flexural-testing.

[24] H. S. Maiti, “Advanced ceramics for strategic applications,” Lectures, Kharagpur, Indian Institute of Technology, Department of Metallurgy and Material Science.

[25]“(https://employees.csbsju.edu/cschaller/Principles%20Chem/network/NWalumina.html) ”

[26] Benjah-bmm27, “Ball-and-stick model of part of the crystal structure of corundum, α-Al_2 O_3.”

[27] “(http://www.quartzpage.de/gen_struct.html).”

[28] A. Abdullayev, M. Bekheet, D. Hanaor, and A. Gurlo, “Materials and Applications for Low-Cost Ceramic Membranes,” *Membranes (Basel)*, vol. 9, no. 9, p. 105, Aug. 2019, doi: 10.3390/membranes9090105.

[29] S. Zha, J. Yu, G. Zhang, N. Liu, and R. Lee, “Polyethersulfone (PES)/cellulose acetate butyrate (CAB) composite hollow fiber membranes for BTEX separation from produced water,” *RSC Adv*, vol. 5, no. 128, pp. 105692–105698, 2015, doi: 10.1039/C5RA21185A.

[30] “(https://www.waterdropfilter.com/).”

[31] “(https://www.freshwatersystems.com).”

[32] "'Sub-nano Ceramic Membrane' Capable of Molecular Separation," (https://www.ngk-insulators.com/en/rd/subnano).

[33] يوسف، بن بريكة, "تحضير ودراسة حوامل لأغشية خزفية انطلاقا من مواد اولية محلية, مذكرة ماستر," جامعة محمد خيضر - بسكرة, بسكرة, 2019.

[34] L. Ansaloni *et al.*, "Upscaling polyPOSS-imide membranes for high temperature H2 upgrading," *J Memb Sci*, vol. 620, p. 118875, Feb. 2021, doi: 10.1016/j.memsci.2020.118875.

[35] M. Hartinger, H.-J. Heidebrecht, S. Schiffer, J. Dumpler, and U. Kulozik, "Technical Concepts for the Investigation of Spatial Effects in Spiral-Wound Microfiltration Membranes," *Membranes (Basel)*, vol. 9, no. 7, p. 80, Jul. 2019, doi: 10.3390/membranes9070080.

Summary

This thesis presents the culmination of a study aimed at elaboration and characterization of local ceramic materials for agricultural microfiltration applications, which in practice meant manufacturing and evaluating the durability microfiltration ceramic tubes. Through rigorous experimentation and analysis, significant findings have emerged.

Chemical analysis revealed notable transformations in the ceramic tubes at 1150℃, an increase in silica content up to 62 $wt\%$ and a phase transition predominantly to the Mullite phase, and as we increase temperature to 1175℃ and 1200℃ a slight increase of this phase occurs as confirmed by X-ray fluorescence (XRF) and X-ray diffraction (XRD).

Mechanical properties analysis demonstrated that tubes treated at higher temperatures exhibited superior flexural and tensile stress values such as $\sigma_F^{1200℃} = 25.164\ MPa$ while $\sigma_F^{1175℃} = 24.732\ MPa$ and $\sigma_F^{1150℃} = 21.789\ MPa$, indicating increased mechanical strength. However, permeability results indicated a negative impact on permeability at higher temperatures, despite the enhanced mechanical strength. $\Phi_{1200℃} = 480\ {}^{l}/_{m^2.h.bar} < \Phi_{1150℃} = 494.1\ {}^{l}/_{m^2.h.bar}$

Filtration tests showcased the efficacy of these filters in removing suspended particles at the microfiltration level, affirming their practical utility in filtration applications.

Overall, these findings contribute valuable insights into the performance and potential applications of ceramic tubes in various industrial and environmental contexts.

Keywords: Kaolin DD1; Kaolin DD3; Calcium Carbonate ($CaCO_3$); Supports; Microfiltration; Extrusion.

ملخص

هذه المذكرة تقدم ختام دراسة تهدف إلى تصنيع وتوصيف مواد خزفية محلية لتطبيقات التنقية الميكرونية في المجالات الزراعية، مما يعني عملياً تصنيع وتقييم أداء حوامل أغشية من السيراميك للتنقية الميكرونية. من خلال التجارب والتحاليل الدقيقة، ظهرت نتائج مهمة.

أظهر التحليل الكيميائي تحولات ملحوظة في أنابيب السيراميك عند 1150 درجة مئوية، زيادة محتوى السيليكا وصولا إلى 62 وزن٪ وانتقال الطور بشكل أساسي من طور الكاولينايت إلى طور المولايت، ومع زيادة درجة الحرارة إلى 1175 درجة مئوية و 1200 درجة مئوية يحدث زيادة طفيفة في هذه الطور اكدت هذه النتائج تحاليل حيود الاشعة السينية وتحليل فلورة الاشعة السينية.

أظهرت دراسة الخصائص الميكانيكية أن الأنابيب التي تم معالجتها عند درجات حرارة أعلى أظهرت قيمًا متفوقة للمقاومة الشد، $\sigma_F^{1200℃} = 25.164\ MPa$ بينما $\sigma_F^{1175℃} = 24.732\ MPa$ و $\sigma_F^{1150℃} = 21.789\ MPa$، مما يشير إلى زيادة في القوة الميكانيكية. ومع ذلك، أظهرت نتائج النفاذية تأثيرًا سلبيًا على النفاذية عند درجات حرارة أعلى، على الرغم من زيادة القوة الميكانيكية حيث ان:

$$\sigma_F^{1175℃} = 24.732\ MPa \text{ and } \sigma_F^{1150℃} = 21.789\ MPa, \sigma_F^{1200℃} = 25.164\ MPa$$

أظهرت اختبارات التنقية كفاءة هذه الحوامل في إزالة الجسيمات المعلقة على مستوى التنقية الميكرونية (Microfiltration)، مما يؤكد فائدتها العملية في تطبيقات التنقية.

بشكل عام، تساهم هذه النتائج في إلقاء نظرة مهمة على الأداء والتطبيقات المحتملة لأنابيب السيراميك في مختلف السياقات العلمية، الصناعية والبيئية.

الكلمات المفتاحية: كاولان DD1؛ كاولان DD3؛ كربونات الكالسيوم ($CaCO_3$)؛ حوامل؛ التنقية الميكرونية؛ البثق.

REPUBLIQUE ALGERIENNE DEMOCRATIQUE ET POPULAIRE
MINISTERE DE L'ENSEIGNEMENT SUPERIEUR
ET DE LA RECHERCHE SCIENTIFIQUE
UNIVERSITE MOHAMED KHIDER - BISKRA
Faculté des SE&SNV
Département des Sciences de la matière
Filière: Physique

الجمهورية الجزائرية الديمقراطية الشعبية
وزارة التعليم العالي والبحث العلمي
جامعة محمد خيضر بسكرة
كلية العلوم الدقيقة وعلوم الطبيعة والحياة
قسم :علوم المادة
شعبة :الفيزياء

تصريـــح شرفـــي

خاص بالالتزام بقواعد النزاهة العلمية لإنجاز بحث

(ملحق القرار 1082 المؤرخ في 2021/12/27)

أنا الممضي أسفله،

السيد(ة): لحميدي أصيل .....

الصفة: طالب سنة ثانية ماستر فيزياء تخصص: فيزياء المادة المكثفة

الحامل(ة) لبطاقة التعريف الوطنية رقم: L00008802 الصادرة بتاريخ: 2019/06/30

المسجل بكلية: العلوم الدقيقة وعلوم الطبيعة والحياة قسم: علوم المادة .....

والمكلف بانجاز أعمال بحث : مذكرة ماستر في الفيزياء

عنوانها: Elaboration and characterization of local ceramic materials for agricultural ammonia filtration application

أصرح بشرفي أني ألتزم بمراعاة المعايير العلمية والمنهجية ومعايير الأخلاقيات المهنية والنزاهة الأكاديمية المطلوبة في انجاز البحث المذكور أعلاه وفق ما ينص عليه القرار رقم 1082 المؤرخ في 2021/12/27 المحدد للقواعد المتعلقة بالوقاية من السرقة العلمية ومكافحتها.

التاريخ: 2024/06/26

إمضاء المعني بالأمر

Assil